

# *STEEP: a remotely-sensed energy balance model for evapotranspiration estimation in seasonally dry tropical forests*

Article

Accepted Version

Bezerra, U. A., Cunha, J., Valente, F., Nóbrega, R. L. B., Andrade, J. M., Moura, M. S.B., Verhoef, A. ORCID: <https://orcid.org/0000-0002-9498-6696>, Perez-Marin, A. M. and Galvão, C. O. (2023) STEEP: a remotely-sensed energy balance model for evapotranspiration estimation in seasonally dry tropical forests. *Agricultural and Forest Meteorology*, 333. 109408. ISSN 0168-1923 doi: <https://doi.org/10.1016/j.agrformet.2023.109408> Available at <https://centaur.reading.ac.uk/111295/>

It is advisable to refer to the publisher's version if you intend to cite from the work. See [Guidance on citing](#).

To link to this article DOI: <http://dx.doi.org/10.1016/j.agrformet.2023.109408>

Publisher: Elsevier

All outputs in CentAUR are protected by Intellectual Property Rights law, including copyright law. Copyright and IPR is retained by the creators or other copyright holders. Terms and conditions for use of this material are defined in

the [End User Agreement](#).

[www.reading.ac.uk/centaur](http://www.reading.ac.uk/centaur)

## **CentAUR**

Central Archive at the University of Reading

Reading's research outputs online

# 1 **STEEP: a remotely-sensed energy balance model for evapotranspiration estimation in** 2 **seasonally dry tropical forests**

3 Ulisses A. Bezerra<sup>a</sup>, John Cunha<sup>a</sup>, Fernanda Valente<sup>b</sup>, Rodolfo L. B. Nóbrega<sup>c,d</sup>, João M. Andrade<sup>e</sup>, Magna  
4 S. B. Moura<sup>f</sup>, Anne Verhoef<sup>g</sup>, Aldrin M. Perez-Marin<sup>h</sup>, Carlos O. Galvão<sup>a</sup>

5 <sup>a</sup>Federal University of Campina Grande, Centre for Natural Resources and Technology, Campina Grande, Brazil

6 <sup>b</sup>Forest Research Centre (CEF), School of Agriculture, University of Lisbon, Tapada da Ajuda, 1349-017 Lisbon, Portugal

7 <sup>c</sup>University of Bristol, School of Geographical Sciences, University Rd, Bristol, BS8 1SS, UK

8 <sup>d</sup>Imperial College London, Georgina Mace Centre for the Living Planet, Department of Life Sciences, Silwood Park  
9 Campus, Buckhurst Road, Ascot, SL5 7PY, UK

10 <sup>e</sup>Federal University of Pernambuco, Department of Civil and Environmental Engineering, Recife, Brazil

11 <sup>f</sup>Empresa Brasileira de Pesquisa Agropecuária, Embrapa Semiárido, Petrolina, Brazil

12 <sup>g</sup>The University of Reading, Department of Geography and Environmental Science, UK

13 <sup>h</sup>Instituto Nacional do Semiárido/Núcleo de Desertificação e Agroecologia, Campina Grande, Brazil

14 \*Corresponding author: ulisses.alencar@estudante.ufcg.edu.br; ulisses.alencar17@gmail.com

## 15 **Highlights**

- 16 • STEEP is a RS-based SEB model from a one-source bulk transfer equation for SDTF.
- 17 • STEEP includes improved representations of phenology and soil moisture for SDTF.
- 18 • STEEP is tested against eddy covariance data from the largest SDTF in South America.
- 19 • STEEP exhibits satisfactory metrics and outperforms SEBAL, MOD16, and PMLv2.

## 20 **Abstract**

21 Improvement of evapotranspiration (ET) estimates using remote sensing (RS) products based on  
22 multispectral and thermal sensors has been a breakthrough in hydrological research. In large-scale  
23 applications, methods that use the approach of RS-based surface energy balance (SEB) models  
24 often rely on oversimplifications. The use of these models for Seasonally Dry Tropical Forests  
25 (SDTF) has been challenging due to incompatibilities between the assumptions underlying those  
26 models and the specificities of this environment, such as the highly contrasting phenological phases  
27 or ET being mainly controlled by soil–water availability. We developed a RS-based SEB model from  
28 a one-source bulk transfer equation, called Seasonal Tropical Ecosystem Energy Partitioning  
29 (STEEP). Our model uses the plant area index to represent the woody structure of the plants in  
30 calculating the moment roughness length. We included the parameter  $kB^{-1}$  and its correction using  
31 RS soil moisture in the calculation of the aerodynamic resistance for heat transfer.

32 Besides,  $\lambda ET$  caused by remaining water availability in endmembers pixels was quantified using the  
33 Priestley-Taylor equation. We implemented the algorithm on Google Earth Engine, using freely  
34 available data. To evaluate our model, we used eddy covariance data from four sites in the Caatinga,  
35 the largest SDTF in South America, in the Brazilian semiarid region. Our results show that STEEP  
36 increased the accuracy of ET estimates without requiring any additional climatological information.  
37 This improvement is more pronounced during the dry season, which, in general, ET for these SDTF  
38 is overestimated by traditional SEB models, such as the Surface Energy Balance Algorithms for Land  
39 (SEBAL). The STEEP model had similar or superior behavior and performance statistics relative to  
40 global ET products (MOD16 and PMLv2). This work contributes to an improved understanding of the  
41 drivers and modulators of the energy and water balances at local and regional scales in SDTF.  
42 Keywords: Sensible heat flux, Aerodynamic resistance for heat transfer, Surface energy balance,  
43 Caatinga, Google Earth Engine

44

## 45 **1. Introduction**

46 Quantifying evapotranspiration (ET) is one of the largest research challenges in hydrology  
47 because ET is driven by a complex combination of atmospheric, vegetation, edaphic, and terrain  
48 characteristics (Wang et al., 2016; Bhattarai et al., 2017). The traditional techniques to quantify ET,  
49 e.g. Bowen ratio or eddy covariance system (EC), are limited to areas up to  $\sim 10 \text{ km}^2$  (Allen et al.,  
50 2011; Anapalli et al., 2016; Mcshane et al., 2017; Mallick et al., 2018; Chu et al., 2021). Over the  
51 past decades, models based on satellite remote sensing (RS) data have been increasingly  
52 developed and applied to estimate ET for multiple temporal and spatial scales (Anderson et al., 2011;  
53 Chen and Liu, 2020). RS-based surface energy balance (SEB) models estimate ET in terms of  
54 energy per unit area (e.g.  $\text{W/m}^2$ ), i.e. by latent heat flux,  $\lambda ET$ , where  $\lambda$  is the latent heat of vaporization  
55 of water (Shuttleworth, 2012; Barraza et al., 2017; Trebs et al., 2021). SEB models obtain  $\lambda ET$  by  
56 subtracting the soil heat ( $G$ ) and sensible heat ( $H$ ) fluxes from the net radiation ( $R_n$ ). Estimates of  $R_n$   
57 obtained with RS data have been improving, and this flux can nowadays be estimated with  
58 acceptable precision (Allen et al., 2011; Ferreira et al., 2020). The  $G:R_n$  ratio can be predicted with  
59 reasonable accuracy through the use of empirical relationships with soil, vegetation, and temperature  
60 characteristics (Bastiaanssen, 1995; Murray and Verhoef, 2007; Allen et al., 2011; Danelichen et al.,

61 2014). Challenges in estimating  $\lambda ET$  as a residual of the energy balance are mostly associated with  
62 the uncertainties in  $H$  (Gokmen et al., 2012; Paul et al., 2014; Mohan et al., 2020a, Mohan et al.,  
63 2020b; Costa-Filho et al., 2021). The bulk heat transfer calculation that is used to compute  $H$  involves  
64 variables related to the temperature gradient and to the aerodynamic resistance for heat transfer  
65 ( $rah$ ). If any of these variables are poorly estimated, the performance of SEB models will be reduced  
66 (Verhoef et al., 1997a, b; Su et al., 2001; Gokmen et al., 2012; Costa-Filho et al., 2021; Liu et al.,  
67 2021; Trebs et al., 2021).

68 The difference between the aerodynamic surface temperature and air temperature ( $dT$ )  
69 drives  $H$ . However, the lack of techniques to measure the aerodynamic surface temperature required  
70 strategies to use the radiometric land surface temperature (LST) as an alternative. Bastiaanssen et  
71 al. (1998), when creating the Surface Energy Balance Algorithms for Land (SEBAL), proposed that  
72  $dT$  can be estimated with a linear relationship on LST. This requires identifying areas with contrasting  
73 extreme conditions in terms of cover and humidity, e.g., dry bare and well-watered soil surfaces,  
74 commonly known as hot/dry and cold/wet endmembers, respectively. The sensible heat transfer  
75 equation in conjunction with the surface energy balance in hot/dry and cold/wet endmembers allows  
76 one to obtain the coefficients of the linear relationship between  $dT$  and LST. Bastiaanssen et al.  
77 (1998) proposed the selection of endmembers by assuming that  $H$  in the cold/wet endmember and  
78  $\lambda ET$  in the hot/dry endmember are zero. However, these assumptions are not necessarily valid  
79 (Singh and Irmak, 2011; Singh et al., 2012). The cold/wet endmember refers to an area with a well-  
80 irrigated crop surface having ground fully covered by vegetation, so it can be assumed that a non-  
81 negligible amount of sensible heat can still be generated by such a surface. Similarly, for the hot/dry  
82 endmember, an area dominated by bare soil, there may be a  $\lambda ET$  resulting from antecedent rainfall  
83 events, hereafter referred to as remaining  $\lambda ET$ . Some studies have quantified  $H$  and  $\lambda ET$  in hot/dry  
84 and cold/wet endmembers (Trezza, 2006; Allen et al., 2007; Singh and Irmak, 2011); they have  
85 shown that this quantification produces a better approximation of daily ET.

86 Based on the Monin-Obukhov similarity theory,  $rah$  is defined as a function of the momentum  
87 ( $z0m$ ) and heat ( $z0h$ ) roughness lengths. Theoretically, the sum of the zero plane displacement  
88 height ( $d0$ ) together with  $z0h$  defines the level of the effective source of sensible heat (Thom, 1972;  
89 Chehbouni et al., 1996; Gokmen et al., 2012) and, therefore,  $z0h$  constitutes one of the most crucial

90 parameters for the accurate calculation of  $H$  (Verhoef et al., 1997a; Su et al., 2001). However, as  
91  $z_0h$  cannot be measured directly, it is commonly calculated via the dimensionless parameter  $kB^{-1}$   
92 formulated to express the excess resistance of heat transfer compared to momentum transfer (Owen  
93 and Thomson, 1963). In RS-based SEB models, oversimplifications are present in the calculation of  
94  $rah$ , e.g. different land use types are represented by the same values for  $z_0h$  (Bastiaanssen et al.,  
95 2005; Allen et al., 2007) and  $kB^{-1}$  (Bastiaanssen et al., 1998), or the values for the aerodynamic  
96 parameters are kept constant in time and space. However, these parameters should not be  
97 considered constant, nor set to zero, because this can lead to large inaccuracies in the estimates of  
98  $H$  (Verhoef et al., 1997a) and, consequently, of  $\lambda ET$  (Liu et al., 2007; Paul et al., 2014; Liu et al.,  
99 2021). Studies have shown that  $kB^{-1}$  typically ranges from 1 to 12, depending on the dominant  
100 surface coverage (Kustas et al., 1989a; Troufleau et al., 1997; Verhoef et al., 1997a; Lhomme et al.,  
101 2000; Su et al., 2001). Studies confirm that if appropriate values of  $kB^{-1}$  are used,  $H$  can be accurately  
102 estimated using LST via the bulk transfer method (Stewart et al., 1994; Su et al., 2001; Jia et al.,  
103 2003; Paul et al., 2013).

104 Another problem with RS-based SEB models is that these methods are imprecise when  
105 applied to non-agricultural environments, such as forests, deserts, sparse savannahs or rangelands,  
106 and riparian systems, because of the heterogeneous nature of the vegetation, terrain, soils, and  
107 water availability in these environments. This causes the flux estimates obtained with the SEB  
108 methods, and the underlying aerodynamic parameters, to be highly variable (Allen et al., 2011;  
109 Gokmen et al., 2012; Barraza et al., 2017; Chen and Liu, 2020; Costa-Filho et al., 2021). This is  
110 especially true in Seasonally Dry Tropical Forests (SDTF) regions, where there is a large spatio-  
111 temporal variation in vegetation density, in vegetation structural parameters such as canopy height,  
112 crown shape and branching, and water availability. SDTF are an important tropical biome and one  
113 of the most threatened ecoregions of the world (Moro et al., 2015; Pennington et al., 2018). SDTF  
114 are broadly defined as forest formations in tropical regions characterised by marked seasonality in  
115 rainfall distribution, resulting in a prolonged dry season that usually lasts five or six months  
116 (Pennington et al., 2009; Paloschi et al., 2020). The most extensive contiguous areas of SDTF are  
117 in the neotropics, comprising more than 60% of the remaining global stands of this vegetation (Miles  
118 et al., 2006; Queiroz et al., 2017). The physiognomies exhibited by SDTF are heterogeneous, with

119 vegetation ranging from tall forests with closed canopies to scrublands rich in succulents and thorn-  
120 bearing plants (Moro et al., 2015; Paloschi et al., 2020). SDTF foliage patterns are adapted to the  
121 intense climate and water seasonality, which is highly dependent on interannual climate variability  
122 (Alberton et al., 2017; Medeiros et al., 2022). The vegetation drops most leaves during the dry  
123 season, and the first rainfall events trigger a rapid leaf growth in the wet season (Alberton et al.,  
124 2017; Paloschi et al., 2020; Medeiros et al., 2022). SDTF are being rapidly degraded (12% between  
125 1980 and 2000), highlighting an urgent priority for their conservation (Moro et al., 2015; Maia et al.,  
126 2020). The risks faced by SDTF mainly stem from anthropogenic disturbance effects, which range  
127 from local habitat loss to global climate change, leading to biodiversity loss and reductions in biomass  
128 (Allen et al., 2017; Maia et al., 2020).

129         Application of SEB models to estimate evapotranspiration over SDTF has been challenging  
130 due to the incompatibility between the existing assumptions of the models and the specificities of  
131 these forests. Precipitation seasonality is the primary phenological regulator of SDTF (Moro et al.,  
132 2016; Campos et al., 2019; Paloschi et al., 2020), and land-cover patterns show distinct intra- and  
133 inter-annual spectral responses (Cunha et al., 2020; Andrade et al., 2021; Medeiros et al., 2022).  
134 Therefore, biophysical remotely-sensed variables, such as Normalized Difference Vegetation Index  
135 (NDVI) and surface albedo, which are usually used to select the endmembers, exhibit high spatial  
136 and temporal variability in SDTF, which causes ET estimates from the SEB models to lack fidelity  
137 (Silva et al., 2019). Selection of suitable roughness parameters such as  $z_{0m}$ ,  $d_0$ , and  $kB^{-1}$  is  
138 important for the correct quantification of the energy balance in SDTF. However, these parameters  
139 are more challenging to obtain in SDTF than for evergreen forests, as in addition to vegetation height,  
140 other characteristics such as plant density, above-ground plant structure and the strong seasonality  
141 of phenology (Alberton et al., 2017; Miranda et al., 2020; Paloschi et al., 2020) have a considerable  
142 effect on the turbulent transfer in these forests. Another key issue is how to verify the results of SEB  
143 methods due to the scarcity, in many regions, of terrestrial observations and the uneven  
144 spatiotemporal distribution of monitoring data. SEB models may not satisfactorily represent ET in  
145 regions with sparse vegetation and high climatic seasonality, such as SDTF (Senkondo et al., 2019;  
146 Laipelt et al., 2021; Melo et al., 2021). The main reason is that these methods have generally been  
147 evaluated and/or parameterized using sites located in other ecosystems and climates in North

148 America, Europe, Australia, East Asia, and in agricultural regions that have characteristics quite  
149 distinct from SDTF (Melo et al., 2021). Therefore, a better quantification of ET, especially in regions  
150 with high climatic seasonality, will help to design better water management policies that will be able  
151 to deal with the effects of climate variability, land use/cover and climate changes (Lima et al., 2021).

152 We hypothesise that a SEB model that improves or considers estimates of  $rah$  via  $z0m$  and  
153  $kB^{-1}$  will improve  $H$  and ET for STDF. To test this assumption, we introduce a novel calibration-free  
154 SEB model based upon a one-source bulk transfer equation, herein referred to as Seasonal Tropical  
155 Ecosystem Energy Partitioning (STEEP). The STEEP model aims to improve  $H$  and ET estimates  
156 for STDF by incorporating the woody structure of plants through the Plant Area Index (PAI), and soil  
157 moisture obtained by remote sensing to help represent the seasonality of the aerodynamic and  
158 surface variables that drive the energy fluxes. To obtain the coefficients of the linear relationship  
159 between  $dT$  and LST its coefficients, we computed  $H$  by the surface energy balance, and the  
160 remaining  $\lambda ET$  through the principle of the Priestley-Taylor equation in the hot/dry and cold/wet  
161 endmembers. STEEP is designed to take advantage of the extensive free database available on the  
162 Google Earth Engine (GEE) cloud computing environment. STEEP is herein evaluated at the field  
163 scale against four flux towers in the Caatinga, the largest continuous SDTF in the Americas.  
164 Additionally, the model was compared with SEBAL and two consolidated global ET products: MOD16  
165 (Mu et al., 2011; Running et al., 2017) and PMLv2 (Zhang et al., 2019).

166

## 167 **2. Methodology**

### 168 2.1 Study areas and respective data

169 The study concerns the Brazilian Caatinga, located between the Equator and the Tropic of  
170 Capricorn (about 3 and 18° south), in the Brazilian semiarid region. It covers an area of about  
171 850,000 km<sup>2</sup> (Silva et al., 2017a; Andrade et al., 2021; Brazil MMA, 2021). The climate in the  
172 Caatinga is characterized by high air temperatures (around 26–30° C) and high potential  
173 evapotranspiration (1,500–2,000 mm/year) coupled with low annual rainfall (300–800 mm/year,  
174 normally concentrated in 3–6 months) with high intra- and inter-annual variability in space and time,  
175 and a long dry season which sometimes lasts up to 11 months in some areas of Caatinga (Moro et  
176 al., 2016; Miranda et al., 2018; Paloschi et al., 2020). The Caatinga vegetation has at least thirteen



177 physiognomies ranging from woods to sparse thorny shrubs, morphologically adapted to resist water  
178 stress and high air temperatures (Araújo et al., 2009; Silva et al., 2017a; Marques et al., 2020;  
179 Miranda et al., 2020), and it has been identified as one of the most biodiverse SDTF regions globally  
180 (Pennington et al., 2006; Santos et al., 2014; Koch et al., 2017). Still, the Caatinga and other SDTF  
181 are among the least studied ecoregions compared to tropical forests and savannas (Santos et al.,  
182 2012; Koch et al., 2017; Tomasella et al., 2018; Borges et al., 2020). Only 1% of the Brazilian  
183 Caatinga area is legally protected (Koch et al., 2017).

184 We used data from four sites located in the Caatinga (Fig. 1 and Table 1). The surrounding  
185 areas of each of our study sites — which exceeds these EC towers footprints — are homogeneously  
186 covered by Caatinga vegetation (Fig. S1). Located on crystalline terrain (Fig. 1a), these Caatinga  
187 sites have soils with highly variable properties, ranging from fertile (those with a clayey texture) to  
188 poor (those soils that are sandier). However, most soils of the SDTF are typically shallow and stony  
189 (i.e. Entisols, Alfisols, and Ultisols; WRB, 2006), retaining water only for a short period between  
190 rainfall events and after the rainy season (Moro et al., 2015; Queiroz et al., 2017). The wet and (dry)  
191 seasons from the sites Petrolina (PTN) are concentrated in Jan–Apr (May–Dec; Souza et al., 2015);  
192 Serra Negra do Norte (SNN) in Jan–May (June–Dec; Marques et al., 2020); Serra Talhada (SET) in  
193 Nov–Apr (May–Oct; Silva et al., 2017b) and Campina Grande (CGR) in Mar–July (Aug–Feb; Oliveira  
194 et al., 2021). The climate of the four observation sites is semi-arid, type BSh (Fig. 1b) according to  
195 the Köppen climate classification (Alvares et al., 2013).

196 Eddy covariance data, covering several periods from 2011 to 2020 (Fig. 1c), were used to  
197 evaluate the modelled ET and  $H$ . The four sites were instrumented with five flux towers equipped  
198 with three-dimensional ultrasonic anemometers (CSAT3, Campbell Scientific Inc., Logan, UT, USA  
199 in all the sites except CGR 2020) and open-path infrared gas analysers (LI-7500, LI-COR Inc.,  
200 Lincoln, NE, USA, in the PTN site, or EC150, Campbell Scientific Inc., Logan, UT, USA, in the SET,  
201 SNN, and CGR 2014 sites). In the more recent experiment (CGR 2020), the flux tower was equipped  
202 with an IRGASON (Campbell Scientific Inc., Logan, UT, USA) that integrates the two sensors in just  
203 one instrument. ET data for the PTN, SNN, and SET sites have been previously described; they  
204 underwent standard procedures to ensure their quality and were published by Melo et al. (2021).  
205 Observations at the CGR site were collected through two micrometeorological towers, located in a

206 dense Caatinga area within the Brazilian National Institute of Semiarid (INSA) experimental area, a  
207 300 ha forest reserve with different stages of regeneration. The first tower (height of 7 m) was active  
208 between the years of 2014 and 2017, as described in Oliveira et al. (2021). The second tower (height  
209 of 15 m) is part of the Caatinga Observatory (OCA) and includes an EC system that has been  
210 collecting data since 2020. The OCA is a laboratory maintained by the Federal University of Campina  
211 Grande and INSA.  $H$  data for the PTN, SNN and CGR sites have been obtained from the respective  
212 principal investigators, while data for the SET site have been obtained from the AmeriFlux network  
213 (Antonino, 2019). For the retrieval of  $\lambda ET$  and  $H$ , LoggerNet software (Campbell Scientific, Inc.,  
214 Logan, UT, USA) was used in order to transform 10 Hz raw data into 30 min binaries. Afterwards,  
215 EdiRe software (Campbell Scientific Inc., Logan, UT, USA) was used to process the high-frequency  
216 data, averaging every 30 min. The data from the EC flow towers in CGR have previously gone  
217 through standard procedures to ensure their quality. Detailed information on data processing, quality  
218 control, and post-processing can be found in Campos et al. (2019) and Cabral et al. (2020). The raw  
219 data from the CGR flux tower were processed by Easy-flux data processing software (Campbell  
220 Scientific Inc., Logan, UT, USA). In addition, data for any day with rainfall greater than 0.5 mm were  
221 removed. The daily ET was calculated using the daily average  $\lambda ET$ .

222

223

224

225

226

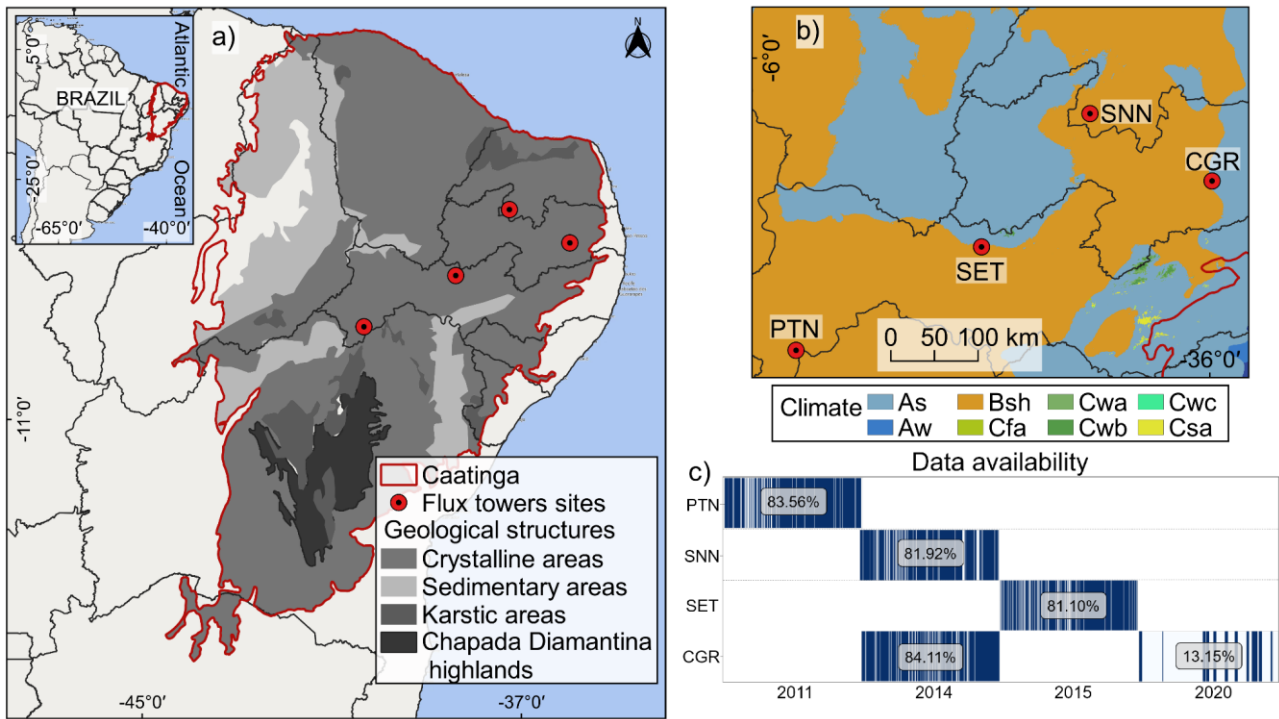
227

228 Table 1. List of EC-equipped flux tower observation sites in the study area.

Sites	State of Brazil	Mean annual of rainfall (mm) <sup>1</sup>	Site average elevation (m)	Main tree species	Location (Lon;Lat)	Data availability	Wet / Dry Seasons	Main reference
Petrolina (PTN)	Pernambuco	428.6	395	<i>Commiphora leptophloeos</i> , <i>Schinopsis brasiliensis</i> , <i>Mimosa tenuiflora</i> , <i>Cenostigma microphyllum</i> , <i>Sapium glandulosum</i>	-40.3212; -9.0465	Jan–Dec 2011	Jan-Apr / May-Dec	Souza et al. (2015)
Serra Negra do Norte (SNN)	Rio Grande do Norte	629.5	205	<i>Caesalpinia pyramidalis</i> , <i>Aspidosperma pyriformis</i> , <i>Anadenanthera colubrina</i> , <i>Croton blanchetianus</i>	-37.2514; -6.5783	Jan–Dec 2014	Jan-May / June-Dec	Marques et al. (2020)
Serra Talhada (SET)	Pernambuco	648	465	<i>Mimosa hostilis</i> , <i>Mimosa verrucosa</i> , <i>Croton sonderianus</i> , <i>Anadenanthera macrocarpa</i> , <i>Spondias tuberosa</i>	-38.3842; -7.9682	Jan–Dec 2015	Nov-Apr / May-Oct	Silva et al. (2017b)
Campina Grande (CGR)	Paraíba	777	490	<i>Croton blanchetianus</i> , <i>Mimosa ophthalmocentra</i> , <i>Poincianella pyramidalis</i> , <i>Allophylus quercifolius</i> , <i>Mimosa sp.</i> <sup>2</sup>	-35.9750; -7.2798	Jan–Dec 2014	Mar-July / Aug-Feb	Oliveira et al. (2021)
Campina Grande (CGR)	Paraíba	777	490	<i>Croton blanchetianus</i> , <i>Mimosa ophthalmocentra</i> , <i>Poincianella pyramidalis</i> , <i>Allophylus quercifolius</i> , <i>Mimosa sp.</i> <sup>2</sup>	-35.9763; -7.2805	Jan–Dec 2020	Mar-July / Aug-Feb	This study

229 <sup>1</sup> Rainfall Data Sources: Brazilian National Institute of Meteorology (INMET) and Pernambuco State Agency for Water and Climate (APAC).

230 <sup>2</sup> Barbosa et al. (2020).



231

232

233

234

235

236

237

238

239

240

241

242

243

244

245

246

247

248

Fig. 1. Location of flux tower observation sites in Caatinga. a) Geographical overview of the

Caatinga (Moro et al., 2015), b) Köppen's climate classification map: Tropical zone with dry summer

(As), Tropical zone with dry winter (Aw), Dry zone semi-arid low latitude and altitude (Bsh), Humid

subtropical zone without dry season and with hot summer (Cfa), Humid subtropical zone with dry

winter and hot summer (Cwa), Humid subtropical zone with dry winter and temperate summer

(Cwb), Humid subtropical zone with dry winter and short and cool summer (Cwc), Humid

subtropical zone with dry summer and hot (Csa), according to Alvares et al. (2013) and c) Data

availability on the observation sites after procedures to ensure their quality.

## 2.2 The Seasonal Tropical Ecosystem Energy Partitioning (STEER) model

SEB models have been applied in many parts of the world (Mohan et al., 2020a). The one-

source SEB models that are most commonly found in the literature are SEBAL (Bastiaanssen et al.,

1998), Surface Energy Balance System (SEBS; Su, 2002), Mapping EvapoTranspiration at high

Resolution with Internal Calibration (METRIC; Allen et al., 2007), and Operational Simplified Surface

Energy Balance (SSEBop; Senay et al., 2013). As in other SEB models, STEER performs the energy

balance at the time of satellite overpass (instantaneous) to obtain  $\lambda ET$  as the surface energy balance

residual. The computation of  $R_n$  and  $G$ , necessary to get  $\lambda ET$ , followed the procedures described in

Ferreira et al. (2020) and Bastiaanssen et al. (2002), respectively, but with input data from the

249 Moderate-Resolution Imaging Spectroradiometer (MODIS) sensor.  $H$  was calculated following the  
250 methods described in Table 2: using  $rah$  and  $dT$ , both traditionally applied in SEB models, but also  
251 focusing on peculiarities of SDTF that have never been considered in other SEB models. In this  
252 proposed version,  $rah$  was described according to Verhoef et al. (1997a) and Paul et al. (2013),  
253 which requires, among other parameters/variables, the momentum roughness length ( $z0m$ ), the zero  
254 plane displacement height ( $d0$ ), the dimensionless parameter  $kB^{-1}$ , and the atmospheric stability  
255 corrections (Paulson, 1970).  $z0m$  is influenced by a range of plant structural properties, e.g.  
256 vegetation height, breadth and vegetation drag coefficients, and spacing (or density).  $z0m$  is  
257 commonly computed as a function of Leaf Area Index (LAI; Verhoef et al., 1997b; Liu et al., 2021).  
258 However, most SDTF plants spend a substantial part of the year without leaves; under these  
259 conditions,  $z0m$  should be derived from information on dimensions of trunks, stems, and branches.  
260 Since LAI is only related to leaf cover quantity and variability, it cannot represent the woody plant  
261 structure without leaves (Miranda et al., 2020). Therefore, the Plant Area Index (PAI), which is the  
262 total above-ground plant area, i.e. leaves and woody structures, was used to represent plant  
263 structures in the computation of  $z0m$  and  $d0$ .

264 To incorporate the conditions of water variability in the forest system in the calculation of  
265 sensible heat we applied the procedure described in Gokmen et al. (2012) that corrects the  $kB^{-1}$   
266 equation presented in Su et al. (2001), incorporating soil moisture obtained by remote sensing. The  
267 canopy conductance profiles are the link between soil moisture and sensible/latent heat flux. The  
268 source of sensible/latent heat moves vertically throughout the canopy as a function of plant water  
269 stress (Gokmen et al., 2012; Bonan et al., 2021), which affects heat roughness length, and, therefore,  
270  $kB^{-1}$  and  $rah$ . Thus, when there is a reduction in soil moisture, there is also a reduction in the value  
271 of  $rah$  and, consequently, an increase of  $H$  and a decrease in  $\lambda ET$ . Furthermore, to calculate  $dT$ , we  
272 used the linear relationship on LST, using the assumption of extreme contrast in terms of cover and  
273 soil wetness (hot/dry and cold/wet endmembers) to determine the linear relationship coefficients.  
274 However, in the hot/dry and cold/wet endmembers pixels,  $H$  was computed by the surface energy  
275 balance (Allen et al., 2007), and the remaining  $\lambda ET$  was incorporated through the Priestley-Taylor  
276 (1972) equation and plant physiological constraints following the approach in Singh and Irmak (2011)  
277 and French et al. (2015). PAI and soil moisture time series used in our study can be seen in Fig. S2.

278 The references for the methods and equations adopted to formulate the STEEP model can be found  
 279 in Table 2 and Appendix A, respectively. For illustration purposes, Table 2 also shows the references  
 280 for the methods for one of the most widely used RS SEB models, the SEBAL model.

281 Table 2. References for the methods used in the STEEP and SEBAL models to obtain the sensible  
 282 heat flux.

Variable/Parameter	STEPP	SEBAL
Aerodynamic resistance for heat transfer ( $rah$ )	Verhoef et al., 1997a; Paul et al., 2013	Bastiaanssen et al., 2002; Laipelt et al., 2021
Roughness length for momentum transfer ( $z0m$ )	Verhoef et al., 1997b; Paul et al., 2013, replacing LAI with PAI	Bastiaanssen et al., 2002; Laipelt et al., 2021
Zero plane displacement height ( $d0$ )	Verhoef et al., 1997b; Paul et al., 2013	-
Plant Area Index (PAI)	Miranda et al., 2020	-
Parameter $kB^{-1}$	Su et al., 2001	uses $z0h$ with constant value (0.1); Bastiaanssen et al., 2002
Correction of soil moisture by remote sensing in $kB^{-1}$	Gokmen et al., 2012	-
Calculation of the $H$ and the remaining $\lambda ET$ in endmembers pixels	Allen et al., 2007; Singh and Irmak, 2011; French et al., 2015	Calculation of the $H$ in the hot/dry endmember only; Bastiaanssen et al., 2002

283

### 284 2.3 Algorithm implementation and processing

285 We implemented STEEP on the Google Earth Engine (GEE) cloud computing environment  
 286 (Gorelick et al., 2017) using the Python API (version 3.6). Statistical analyses to evaluate the  
 287 performance of the models were also conducted in Python and implemented in the Jupyter  
 288 programming environment. The Python package geemap (Wu, 2020) enabled the integration of  
 289 Python with the GEE environment, and the hydrostats package (Roberts et al., 2018) was used for  
 290 the statistical evaluation of the performance of the models.

291 We designed the application of the model to take advantage of the data available on GEE  
 292 (Table 3). The remote sensing datasets were derived from MODIS sensor products, the Shuttle  
 293 Radar Topography Mission (SRTM; Farr et al., 2007), and the Global Forest Canopy Height product  
 294 provided vegetation height (Potapov et al., 2021). The climate data necessary to run the model, i.e.  
 295 wind speed, air temperature, relative humidity, shortwave radiation, and net thermal radiation at the  
 296 surface, were sourced from the ERA5-Land reanalysis product (Muñoz Sabater, 2019). For data

297 regarding soil moisture, we used the Global Land Data Assimilation System (GLDAS) product  
 298 (Rodell et al., 2004). CHIRPS precipitation product (Funk et al., 2015) was used to estimate the daily  
 299 rainfall amount at the sites evaluated.

300 Table 3. Description of the datasets available on the GEE platform used in the research.

Product	GEE ID	Bands/variables	Time coverage	Spatial resolution	Temporal resolution
MCD43A4.006	MODIS/006/ MCD43A4	B1–B7	Feb 2000– present	0.5 km	1 day
MOD09GA.006	MODIS/006/ MOD09GA	SolarZenith	Feb 2000– present	1 km	1 day
MOD11A1.006	MODIS/006/ MOD11A1	LST_Day_1km; Emis_31, Emis_32	Mar 2000– present	1 km	1 day
SRTM	USGS/SRT MGL1_003	Elevation	Feb 2000	0.03 km	-
ERA5-Land	ECMWF/ER A5_LAND/H OURLY	dewpoint_temperature_2m, temperature_2m, u_component_of_wind_10, v_component_of_wind_10m, surface_net_solar_radiation _hourly, surface_net_thermal_radiati on_hourly	Jan 1981– present	0.1°	1 h
GLDAS	NASA/GLDA S/V021/NOA H/G025/T3H	SoilMoi0_10cm_inst	Jan 2000– present	0.25°	3 h
Global Forest Canopy Height, 2019	users/potapo vpeter/GEDI _V27	-	Apr 2019	0.03 km	-
CHIRPS	UCSB- CHG/CHIRP S/DAILY	Precipitation	Jan 1981– present	0.05°	1 day
MOD16A2.006	MODIS/006/ MOD16A2	ET	Jan 2001– present	0.5 km	8 days
PML_V2	projects/pml _evapotrans piration/PML /OUTPUT/P ML_V2_8da y_v016	Es, Ec, Ei	Feb 2000– present	0.5 km	8 days

301  
 302 The presence of clouds or instrumental malfunctioning of orbital sensors can cause gaps in  
 303 data. To reduce the loss of information due to missing data, we chose to use the MODIS MCD43A4



304 reflectance product. By combining reflectance data from MODIS sensors aboard the AQUA and  
305 TERRA satellites and modelling the anisotropic scattering characteristics using sixteen-day quality  
306 observations, the MCD43A4 product represents the daily dynamics of the Earth's surface without  
307 missing data (Schaaf and Wang, 2015). Daily surface reflectance data from the MCD43A4 product  
308 were used to obtain the surface albedo and vegetation indices (NDVI and PAI) needed to run STEEP.  
309 Thus, the surface albedo data and the vegetation indices show a low percentage of missing data.  
310 To compose the LST time series, we used data from MOD11A1, and to fill its missing data, a filter  
311 with the average value for a monthly window was applied. This procedure is similar to the method  
312 proposed by Zhao et al. (2005) and it is also used by the MOD16 algorithm to generate the  
313 continuous global ET (Mu et al., 2011).

314         Following the approach in comparable studies, STEEP algorithm processing was conducted  
315 with automatic selection of endmembers pixels (Bhattarai et al., 2017; Silva et al., 2019; Laipelt et  
316 al., 2021). Like Silva et al. (2019), we used the biophysical variables NDVI, surface albedo and LST  
317 to automate selection of the endmembers, but we applied different criteria. For the hot/dry  
318 endmember selection, the first step consisted of selecting those pixels whose surface albedo values  
319 are between the 50 and 75% quantiles, and with NDVI values greater than 0.1 and less than the  
320 15% quantile. After this first selection, a refinement is applied by selecting only those pixels from this  
321 first set that have LST values between the 85 and 97% quantiles. Using the set of pixels that met  
322 these criteria, the median values of  $R_n$ ,  $G$ , LST and  $rah$  were calculated to establish a single value  
323 for each variable and describe the characteristics of the hot pixel. We applied a similar procedure to  
324 select the cold/wet endmember but with different limits (Table 4). The procedure for finding  
325 endmembers was conducted daily. To execute the model and conduct the selection of endmembers,  
326 we used an area of interest (AOI), also known as domain size. AOI was defined as a square area  
327 with 1000-km sides within the Caatinga domain and centred on the tower coordinates of each site.  
328 Cheng et al. (2021), for example, applied the SEBAL using MODIS data in China and used an AOI  
329 of 1200-km x 1200-km.

330                     Table 4. Methodology used for the selection of endmembers pixels.

---

Endmembers
------------

---

	Hot/dry pixel	Cold/wet pixel
Step 1	Q50% < surface albedo < Q75% and 0.10 < NDVI < Q15%	Q25% < surface albedo < Q50% and NDVI > Q97%
Step 2	of the pixels of the 1st Step, select pixels with Q85% < LST < Q97%	of the pixels of the 1st Step, select pixels with LST < Q20%
Step 3	Of the set of pixels that met the previous steps, the median values of $R_n$ , $G$ , LST and $rah$ were calculated to establish a single value for each variable and describe the characteristics of endmembers	

331 Q = quantile.

## 332 2.4 Analysis of the algorithms' performance

333 We used SEBAL as a reference RS SEB model for comparison with STEEP. SEBAL is one  
334 of the most applied SEB models since the algorithm uses a minimal number of in situ measurements  
335 compared to similar models, e.g. METRIC and SSEBop, and is considered a suitable choice for  
336 evapotranspiration estimates over cropped areas and in the context of water resource management  
337 (Kayser et al., 2022). Applications with SEBAL have been conducted in the Caatinga as in the studies  
338 of Teixeira et al. (2009), Santos et al. (2020), Costa et al. (2021), and Lima et al. (2021).  
339 Implementations of the SEBAL algorithm are popular on several computing platforms, e.g. GRASS-  
340 Python (Lima et al., 2021); Google Earth Engine (Laipelt et al., 2021); Python (Mhaweji et al., 2020),  
341 following the formulations described in Bastiaanssen et al. (1998) and Bastiaanssen et al. (2002).  
342 The SEBAL version implemented in this work followed those presented by Bastiaanssen et al.  
343 (2002), Costa et al. (2021) and Laipelt et al. (2021). The remote sensing datasets and endmembers  
344 pixels selection for SEBAL were the same as described in STEEP.

345 ET and  $H$  estimates from STEEP and SEBAL were evaluated against the eddy covariance  
346 measurements of the corresponding tower. Here, the modelled values were extracted for the pixel  
347 representing the EC tower for each observation site. The footprint fetches for PTN, SET, SNN is less  
348 than 500 m (Silva et al., 2017b; Campos et al., 2019; Santos, et al., 2020). We assume a similar  
349 footprint for CGR due to its similarity in terms of wind characteristics and terrain slope compared to  
350 the other sites. Moreover, the surrounding areas of each of our study sites (Fig. S1) — which exceeds  
351 these EC towers footprints — are homogeneously covered by Caatinga vegetation. We evaluated  
352 daily ET values, and instantaneous hourly  $H$  values more specifically with the modelled/measured  $H$

353 value at 11:00 am local time (GMT-3), considering this is the closest time to the satellite's overpass.  
354 Additionally, the STEEP model was compared with two consolidated global ET products available  
355 on GEE: MODIS Global Terrestrial Evapotranspiration A2 version 6 (MOD16; Mu et al., 2011;  
356 Running et al., 2017) and Penman-Monteith-Leuning model version 2 global evaporation (PMLv2;  
357 Zhang et al., 2019); both products have a pixel resolution of 500 m (Table 3). The algorithm used in  
358 MOD16 is based on the Penman-Monteith equation and driven by MODIS remote sensing data with  
359 Modern-Era Retrospective analysis for Research and Applications (MERRA; Mu et al., 2011). In  
360 MOD16 ET is the sum of soil evaporation ( $E_s$ ), canopy transpiration ( $T_c$ ) and wet-canopy evaporation  
361 ( $E_c$ ) and is provided as eight-day *cumulative* values. More details about MOD16 can be found in Mu  
362 et al. (2011) and Running et al. (2017). The global PMLv2 product involves a biophysical model  
363 based on the Penman-Monteith-Leuning equation which also uses MODIS remote sensing data, but  
364 with meteorological reanalysis data from GLDAS as model inputs. As in MOD16, ET in PMLv2 is  
365 also the sum of  $E_s$ ,  $T_c$  and  $E_c$  but is provided as eight-day *average* values. To make MOD16 and  
366 PMLv2 values compatible, ET of PMLv2 was multiplied by eight. Details about PMLv2 can be found  
367 in Gan et al. (2018) and Zhang et al. (2019). We accumulated the daily ET measured at the  
368 observation sites, i.e. derived from EC data, and ET modelled with STEEP for the same eight-day  
369 time periods to make them compatible with the temporal resolution of the MOD16 and PMLv2  
370 datasets. The average of the measured daily values over each eight-day time period (even if there  
371 were missing values within this period) was multiplied by eight to calculate the observed 8-day ET.  
372 To match the time steps of STEEP and MOD16/PMLv2 ET values, the 8-day average of the  
373 evaporative fraction (EF) was multiplied by the daily net radiation over those 8 days, assuming that  
374 EF can be considered constant in each of these periods. Then the ET was summed over the 8-day  
375 interval. Finally, we also compared the modelled ET (by STEEP and the two global products) with  
376 the observed ET, only in the 8-day periods when no field-observed data was missing. However, with  
377 this criterion the number of observations dropped dramatically.

378 The STEEP and SEBAL models and global ET products were evaluated with five performance  
379 metrics (Table 5). A combination of performance metrics is often used to assess the overall  
380 performance of models because a single metric provides only a projection of a certain aspect of the  
381 error characteristics (Chai and Draxler, 2014). Root mean square error (*RMSE*) is commonly used

382 to express the accuracy of the results with the advantage that it presents error values in the same  
383 units of the variable analysed; optimal values are close to zero (Hallak and Pereira Filho, 2011).  
384 Coefficient of determination ( $R^2$ ) represents the quality of the linear trend between observed and  
385 simulated data and ranges from 0 to 1; high values indicate better model performance. Nash–  
386 Sutcliffe efficiency ( $NSE$ ) indicates the accuracy of the model output compared to the average of the  
387 referred data ( $NSE = 1$  is the optimal value; Nash and Sutcliffe, 1970). Concordance correlation  
388 coefficient ( $\rho c$ ) is a measure that evaluates how well bivariate data falls on the 1:1 line.  $\rho c$  measures  
389 both precision and accuracy. It ranges from -1 to +1 similar to Pearson's correlation coefficient, with  
390 perfect agreement at +1 (Lin, 1989; Liao and Lewis, 2000; Akoglu, 2018). Percentage bias ( $PBIAS$ )  
391 measures the average relative difference between observed and estimated values, with an optimal  
392 value of 0 (Gupta et al., 1999). Additionally, we evaluate STEEP's model structure by extracting  
393 model's performance metrics after excluding it from its main implementations individually (Table 2)  
394 and by two-by-two combinations of  $zOm$ ,  $rah$  and  $r\lambda ET$ . We run the control version of the SEB model,  
395 i.e. SEBAL in our case, while incorporating one or two improvements in the model and keeping the  
396 remaining parts of the algorithm the same as the reference SEB model.

397 Table 5. Performance metrics used to evaluate ET and  $H$  in this study.

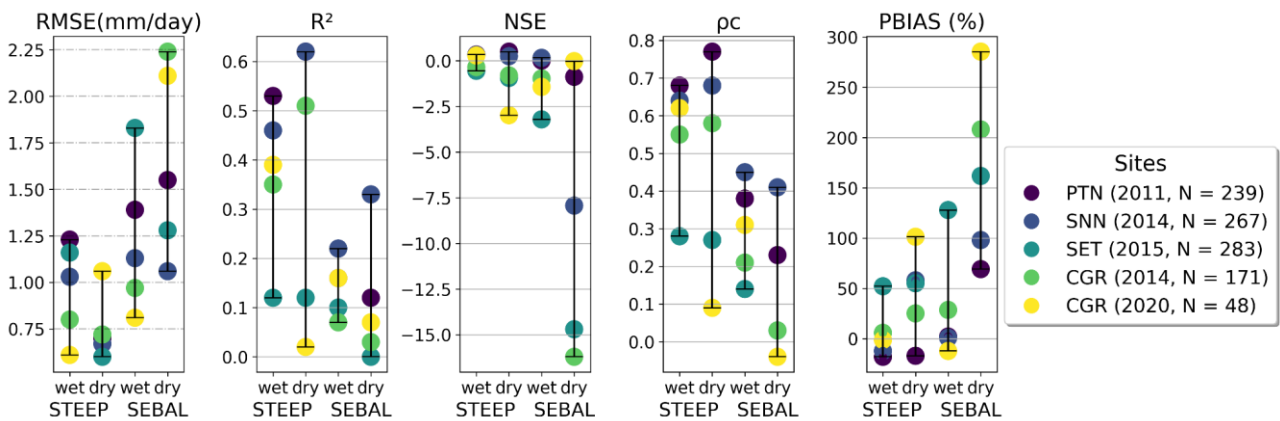
Performance metric	Equation	Range (Perfect value)
Root mean square error ( $RMSE$ )	$RMSE = \sqrt{\frac{\sum_{i=1}^N (M_i - O_i)^2}{N}}$	$[0, +\infty [ (0)$
Coefficient of determination ( $R^2$ )	$R^2 = \frac{[\sum_{i=1}^N (O_i - \bar{O})(M_i - \bar{M})]^2}{\sum_{i=1}^N (O_i - \bar{O})^2 \cdot \sum_{i=1}^N (M_i - \bar{M})^2}$	$[0, 1] (1)$
Nash–Sutcliffe efficiency ( $NSE$ )	$NSE = 1 - \frac{\sum_{i=1}^N (M_i - O_i)^2}{\sum_{i=1}^N (O_i - \bar{O})^2}$	$] -\infty, 1] (1)$
Concordance correlation coefficient ( $\rho c$ )	$\rho c = \frac{2 \sum_{i=1}^N (O_i - \bar{O})(M_i - \bar{M})}{\sum_{i=1}^N (O_i - \bar{O})^2 + \sum_{i=1}^N (M_i - \bar{M})^2 + (N - 1)(\bar{O} - \bar{M})^2}$	$[-1, 1] (1)$
Percentage bias ( $PBIAS$ )	$PBIAS = \frac{\sum_{i=1}^N (M_i - O_i) \cdot 100}{\sum_{i=1}^N O_i}$	$] -\infty, +\infty [ (0)$

398 where:  $N$  sample size;  $O$  observed value;  $M$  modelled value;  $\bar{O}$  observed mean;  $\bar{M}$  modelled mean.

### 399 3. Results and discussion

#### 400 3.1 Comparison of STEEP and SEBAL models results with observed (EC) values

401 The performance statistics of daily ET by STEEP and SEBAL in wet and dry seasons for the  
 402 evaluated sites are shown in Fig. 2. In general, STEEP exhibited a better performance than SEBAL.  
 403 Although the better statistical metrics of STEEP were in the dry season, in the wet season, they were  
 404 also superior compared to SEBAL. Specifically, in the dry season, STEEP exhibited a *RMSE*  
 405 between 0.6 and 1.06 mm/day, while SEBAL this was between 1.06 and 2.24 mm/day. The maximum  
 406 value of  $R^2$  in STEEP was 0.62 (sites PTN and SNN), whereas SEBAL achieved only 0.33. The *NSE*  
 407 metric was the worst among the five analysed in SEBAL: values lower than -7.5 occurred in three of  
 408 the five sites. Although in STEEP, PTN and SNN sites *NSE* had values higher than 0 (0.55 and 0.25,  
 409 respectively) the other sites also had negative values, reaching up to -2.5. In terms of  $\rho_c$ , values  
 410 ranged from 0.09 to 0.77 in STEEP and from -0.04 to 0.41 in SEBAL. It is also possible to see the  
 411 reduction that STEEP has brought to ET modelling in terms of *PBIAS* when compared to SEBAL.  
 412



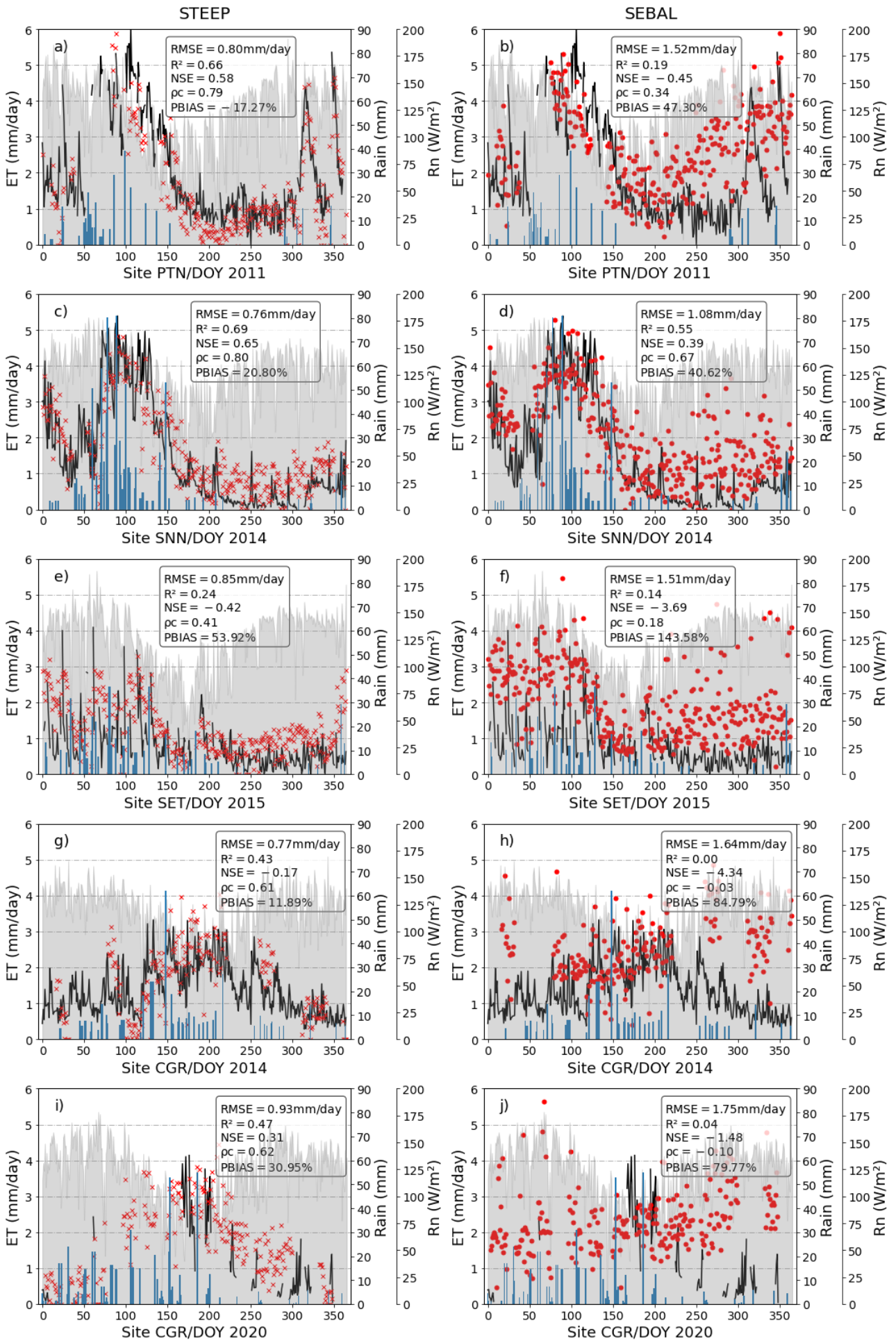
413  
 414 Fig. 2. Results of the performance statistics of daily ET in wet and dry seasons for evaluated sites.

415 Globally, without discriminating between wet and dry seasons, STEEP exhibited better  
 416 statistical performance than SEBAL at all the evaluated sites (Fig. 3). While STEEP exhibited a  
 417 *RMSE* between 0.75 and 0.94 mm/day, the *RMSE* for SEBAL was between 1.08 and 1.75 mm/day.  
 418 In terms of  $R^2$ , the values were between 0.24 to 0.69 for STEEP, and were below 0.2 for SEBAL for  
 419 all sites except in SNN (0.55). Similarly, *NSE* and  $\rho_c$  values were higher for STEEP compared to  
 420 SEBAL. For STEEP, all sites had *NSE* and  $\rho_c$  values above -0.42 and 0.41, respectively, whereas  
 421 all sites except SNN had values below these limits for SEBAL. Both models overestimated ET  
 422 ( $PBIAS > 0$ ), with the exception of the STEEP estimates for the PTN site. The highest overestimation  
 423 by the STEEP model was less than 60%, whereas in SEBAL it was greater than 140%.

424 SEBAL metrics concerning the modelled ET were similar to those found in other studies.  
425 Laipelt et al. (2021) found  $R^2$  ranging from 0.18 to 0.87 when applying SEBAL and comparing it with  
426 data from ten EC towers located in different Brazilian biomes (Amazon, Cerrado, Pantanal, and  
427 Pampa). Cheng et al. (2021) obtained  $R^2$  of 0.53–0.77 and  $RMSE$  of 0.89–1.02 mm/day when  
428 comparing estimates from SEBAL and EC towers on different land covers in China. Costa et al.  
429 (2021), when applying SEBAL in the Caatinga, found  $R^2$  and  $NSE$  values of 0.57 and 0.36,  
430 respectively. Santos et al. (2020) modelled ET with SEBAL at the SNN site for the 2014–2016 period  
431 and obtained  $R^2$  and  $RMSE$  values of 0.28 and 1.43 mm/day, respectively. For this site, we obtained  
432  $R^2$  and  $RMSE$  of 0.55 and 1.08 mm/day, respectively, for the year 2014 using SEBAL.

433 STEEP exhibited a greater seasonal accuracy compared to SEBAL (Fig. 3), as evidenced by  
434 the goodness-of-fit between simulated and observed values expressed by the  $NSE$  indicator. STEEP  
435 estimates followed the same temporal evolution as the observed values. STEEP satisfactorily  
436 captured both minimum and maximum ET values, including after rainfall events, this is particularly  
437 evident in Fig. 3a, where the two observed ET peaks in late 2011 — between DOY 300 and 360 —  
438 in the PTN site were captured nicely by STEEP. This improved performance can be explained  
439 because soil moisture is incorporated in the STEEP algorithm. In semi-arid regions and particularly  
440 in the SDTF, besides the availability of energy, evapotranspiration is highly dependent on the soil–  
441 water availability (Lima et al., 2012; Carvalho et al., 2018; Mutti et al., 2019; Paloschi et al., 2020).  
442 In rainy months, low daily ET rates are often observed due to the reduced levels of incoming radiation  
443 caused by high cloud cover (Mutti et al., 2019; Paloschi et al., 2020). Towards the end of the wet  
444 period, when the available energy increases, the daily ET values also increase as a result of the high  
445 soil water availability from previous precipitation events (Allen et al., 2011; Marques et al., 2020). In  
446 the transition period from the rainy to the dry season, the leaves do not fall immediately (see Table  
447 1, main tree species). Instead, leaf-shedding depends on the environmental conditions in each  
448 location, including the rainy season duration, and species composition (Lima and Rodal, 2010; Lima  
449 et al., 2012; Miranda et al., 2020; Paloschi et al., 2020; Queiroz et al., 2020; Medeiros et al., 2022).  
450 The remaining water available in the soil or previously accumulated in plant tissues is sufficient for  
451 the Caatinga vegetation to maintain its leaves, for short periods, at levels similar to the rainy season  
452 (Barbosa et al., 2006; Mutti et al., 2019). However, in the dry season, when soil moisture reaches its

453 lowest levels, the Caatinga vegetation enters a state of dormancy that is accompanied by leaf drop  
454 and a drastic reduction of photosynthetic activity (and hence of transpiration) as a strategy to cope  
455 with the lack of available soil moisture (Dombroski et al., 2011; Paloschi et al., 2020). This resilience  
456 mechanism is typical of xerophytic and/or deciduous species such as those found in the Caatinga  
457 (Lima et al., 2012; Mutti et al., 2019; Paloschi et al., 2020), and explains the low rates of ET in the  
458 dry season. In contrast, in SEBAL, which does not consider water availability, it was observed that  
459 the daily ET followed the course of the daily net radiation throughout the year, especially in the dry  
460 period of each of the experimental sites. This is in agreement with the results of Kayser et al. (2022),  
461 who pointed out that estimates with SEBAL can be seasonally accurate in locations where the main  
462 driver of ET is the available energy. Our results highlight that SEB models such as SEBAL, which  
463 are formulated to be mainly dependent on energy availability and do not consider soil and plant water  
464 availability, may not satisfactorily represent ET in semi-arid vegetation such as that found in the  
465 SDTF (Gokmen et al., 2012; Paul et al., 2014; Melo et al., 2021).



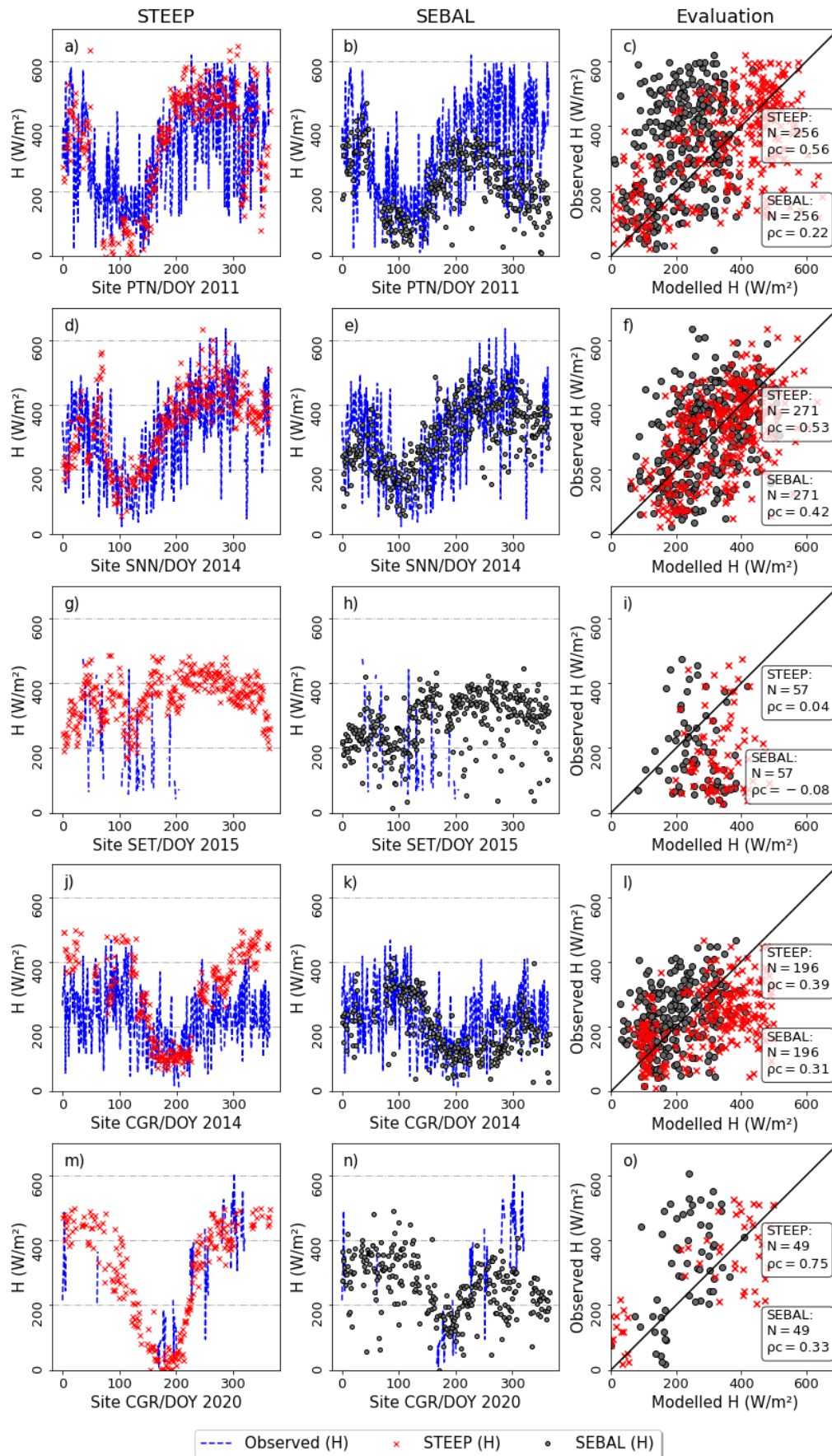
— Observed ET    × STEEP    • SEBAL    ■ RAIN - CHIRPS    ■ Daily net radiation



467 Fig. 3. Observed and modelled daily evapotranspiration (ET, mm/day) for the different  
468 experimental sites: a) and b) PTN 2011, c) and d) SNN 2014, e) and f) SET 2015, g) and h) CGR  
469 2014, i) and j) CGR 2020. The black lines represent observed ET; the red crosses and points are  
470 STEEP and SEBAL estimates, respectively; the blue bars represent CHIRPS daily rainfall; the gray  
471 region represents daily net radiation from ERA5-land.

472 The core of the STEEP and SEBAL algorithms is based on finding  $\lambda ET$  as the residual of the  
473 energy balance; however, they differ with regards to the approach used to calculate  $H$ . In the STEEP  
474 model, the seasonal variation of  $H$  fitted the observed values of the instantaneous measurements at  
475 11:00 am (local time) better than SEBAL, for all the sites (Fig. 4). Our results show that an  
476 improvement in  $H$  leads to a correspondent in ET estimates. This is contrary to the findings of Faivre  
477 et al. (2017), who used the same formulation for  $kB^{-1}$  applied in our study, but included four different  
478 methods to compute  $z0m$ . While STEEP estimates of  $H$  exhibited  $\rho c$  values over 0.5 for three of the  
479 five sites, SEBAL  $H$  estimates exhibited  $\rho c$  values below 0.5 for all sites. When wet and dry seasons  
480 data are analysed separately (Fig. 5), the same trend is observed in the results: in general, the  
481 STEEP model presents better statistical metrics than SEBAL.

482



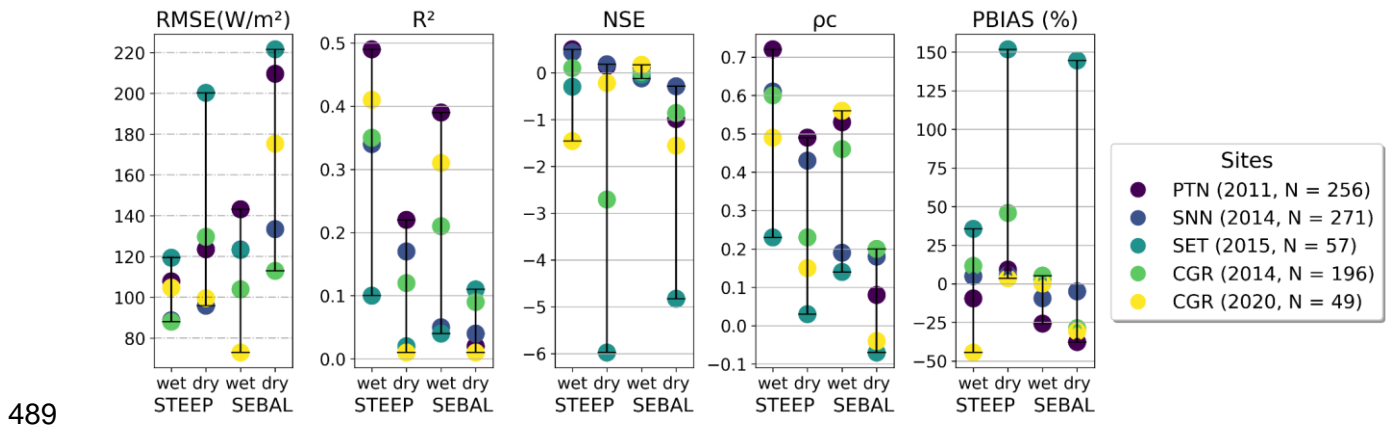
483

484

485

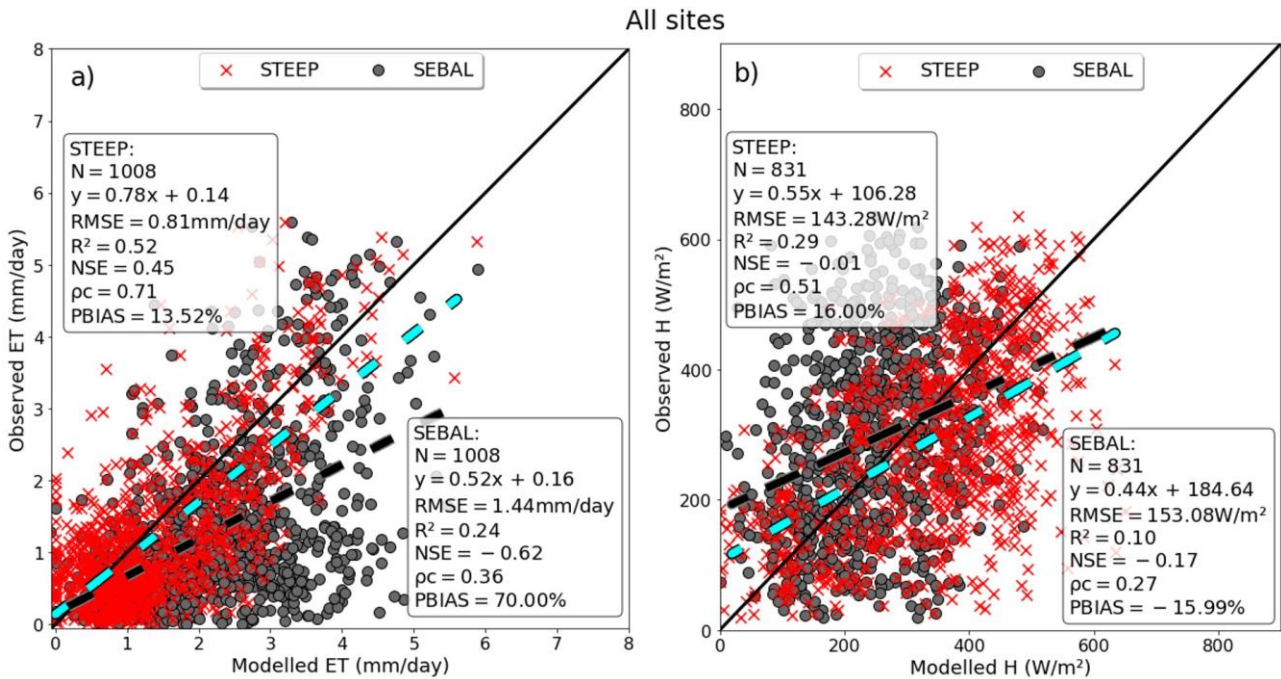
Fig. 4. Observed and modelled instantaneous sensible heat flux ( $H$ , at 11:00 am,  $\text{W/m}^2$ ) for the different experimental sites: a), b) and c) PTN 2011, d), e) and f) SNN 2014, g), h) and i) SET

486 2015, j), k) and l) CGR 2014, m), n) and o) CGR 2020. The blue line represents the observed  
 487 values; the red crosses and grey points correspond to the STEEP and SEBAL estimates,  
 488 respectively. The black line is the 1:1 line.



489  
 490 Fig. 5. Results of the performance statistics of instantaneous sensible heat flux ( $H$ , at 11:00 am,  
 491  $W/m^2$ ) in wet and dry seasons, for the evaluated sites.

492 Evaluation of the STEEP and SEBAL daily ET and instantaneous  $H$  for all experimental sites  
 493 (Fig. 6) indicates that both models lack a high performance for  $H$  estimates, although the use of  
 494 STEEP resulted in better statistical measures than when SEBAL was employed (Fig. 6b). This  
 495 substantiates previous findings (Gokmen et al., 2012; Paul et al., 2014; Trebs et al., 2021), that have  
 496 shown the tendency of underestimation (overestimation) of  $H$  (ET) at water-limited sites. It can be  
 497 seen that the overestimation of  $H$  by the STEEP model, compared to SEBAL, produced modelled  
 498 ET values that were closer to the EC measurements (see Fig. 3 and 4). We ascribe the poor  
 499 performance of  $H$  in the models relative to observed data to the continuous  $H$  oscillations throughout  
 500 the day (Campos et al., 2019; Lima et al., 2021). As we compare an instantaneous  $H$  estimate  
 501 (STEEP or SEBAL) to the 30-min  $H$  average measurement (EC), it is expected that modelled  $H$   
 502 performs worse than daily ET for the same site and period. Furthermore, for sites with fewer  
 503 observations of  $H$  (SET 2015 and CGR 2020), especially in the dry season, the metrics showed that  
 504 STEEP did not perform as well, for each season, as other sites with more data available. Still, these  
 505 limited data were sufficient to show that STEEP outperformed SEBAL in estimating  $H$ .

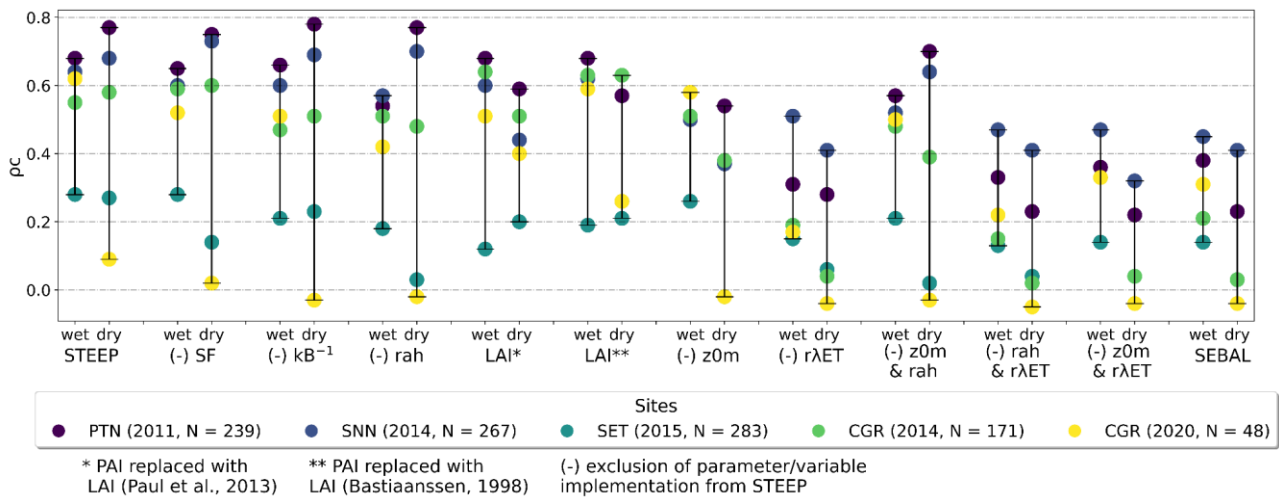


507

508 Fig. 6. Evaluation of observed and modelled: (a) daily evapotranspiration (ET, mm/day) and (b)  
 509 instantaneous sensible heat flux ( $H$ , at 11:00 am, W/m<sup>2</sup>) for all experimental sites. STEEP (red  
 510 crosses) and SEBAL (black points). The black line is the 1:1 line; the cyan (black) dashed line is  
 511 the fitted linear regression between observed and STEEP (SEBAL) model values.

512 We attribute the better performance of STEEP over SEBAL for the Brazilian Caatinga to at  
 513 least three reasons, shown in order of impact of model implementation on its performance (Fig. 7  
 514 and Table S1). First, by quantifying the remaining  $\lambda ET$  in the endmembers pixels through the  
 515 Priestley-Taylor equation, a more reliable estimate of  $H$  in the endmembers pixels can be obtained,  
 516 as was also evidenced by Singh and Irmak (2011). This process is critical for the subsequent  
 517 numerical calculation of  $H$  in SEB models that use  $dT$ , as its accuracy is closely related to quantifying  
 518 the energy balance at the hot and cold endmembers (Trezza, 2006; Allen et al., 2007; Singh and  
 519 Irmak, 2011; Singh et al., 2012). Secondly, roughness characteristics near the surface where the  
 520 heat fluxes originate are parameterised by  $z0m$ , which depends on several factors, such as wind  
 521 direction, height and type of the vegetation cover (Kustas et al., 1989b). Estimation of  $z0m$  only with  
 522 an exponential relationship, as a function of vegetation indices, may be an oversimplification (Kustas  
 523 et al., 1989a; Paul et al., 2013). In our study,  $z0m$  and  $d0$  are calculated with the equations and  
 524 coefficients proposed in Raupach (1994) and Verhoef et al. (1997b), and using PAI because this

525 index better represents the intra-annual phenological changes in the Caatinga (Miranda et al., 2020).  
 526 This procedure considers the characteristics of SDTF, such as seasonality of phenology and  
 527 vegetation height, that considerably affect the quantification of turbulent transfer (Liu et al., 2021).  
 528 Third, our study uses the equation described in Verhoef et al. (1997a) and Paul et al. (2013) to  
 529 estimate *rah*, which considers the differences between heat and momentum transfer, unlike the  
 530 original equation employed in other SEB models e.g. SEBAL or METRIC that only considers *z0m*  
 531 and sets *z0h* = 0.1 when computing this resistance. Furthermore, we account for the  $kB^{-1}$  parameter  
 532 that varies in space and time and incorporates the soil moisture content obtained by RS (Su et al.,  
 533 2001; Gokmen et al., 2012). ET estimation is best represented with a spatially varying  $kB^{-1}$  values,  
 534 as pointed out by the studies of Gokmen et al. (2012) and Paul et al. (2014). Long et al. (2011) report  
 535 that the introduction of these fixed values (*z0h* or  $kB^{-1}$ ) has a significant impact on the magnitudes of  
 536 the estimates of H. Furthermore, Mallick et al. (2018) and Trebs et al. (2021) indicate that the  
 537 parameterization of *rah* can influence the estimation of ET, especially in SEB models that are largely  
 538 dependent on *rah*. Our results show that including just one or two of the refinements had only partial  
 539 performance gains (Fig. 7 and Table S1). In contrast, all the proposed STEEP improvements when  
 540 implemented together resulted in the best performance metrics for all sites.



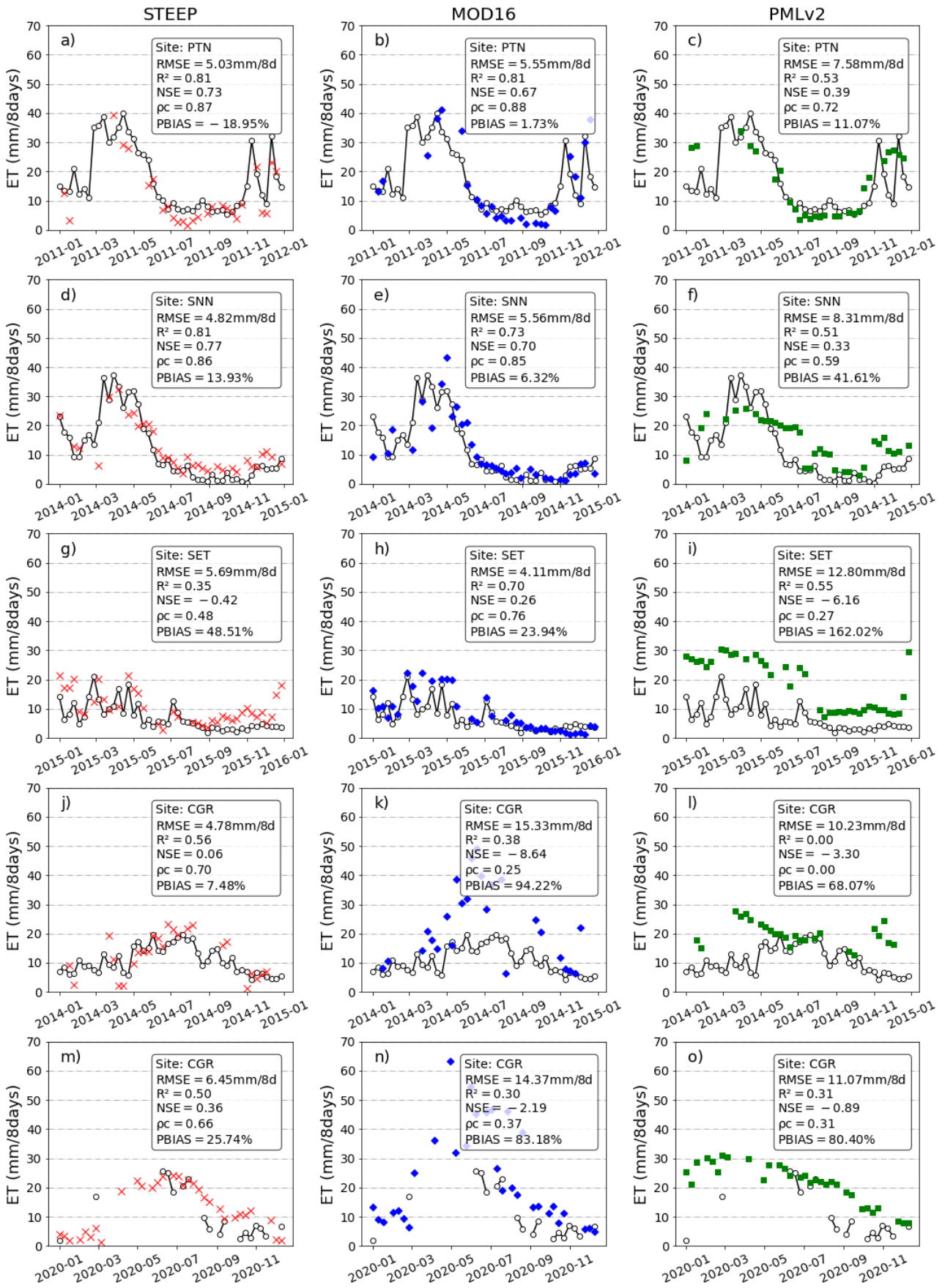
542 Fig. 7. Change of the concordance correlation coefficient ( $\rho_c$ ) by the exclusion/modification of one  
 543 or two parameters/variables implemented in the STEEP model, in the wet and dry seasons: scale  
 544 factor soil moisture correction (SF), the parameter  $kB^{-1}$ , the aerodynamic resistance for heat  
 545 transfer (*rah*), PAI replace with LAI (determined by two different methods), the roughness length for  
 546 momentum transport (*z0m*) and the residual latent heat flux in the end members pixels (*rλET*).

### 547 3.2 Comparison of STEEP model estimates with global evapotranspiration products

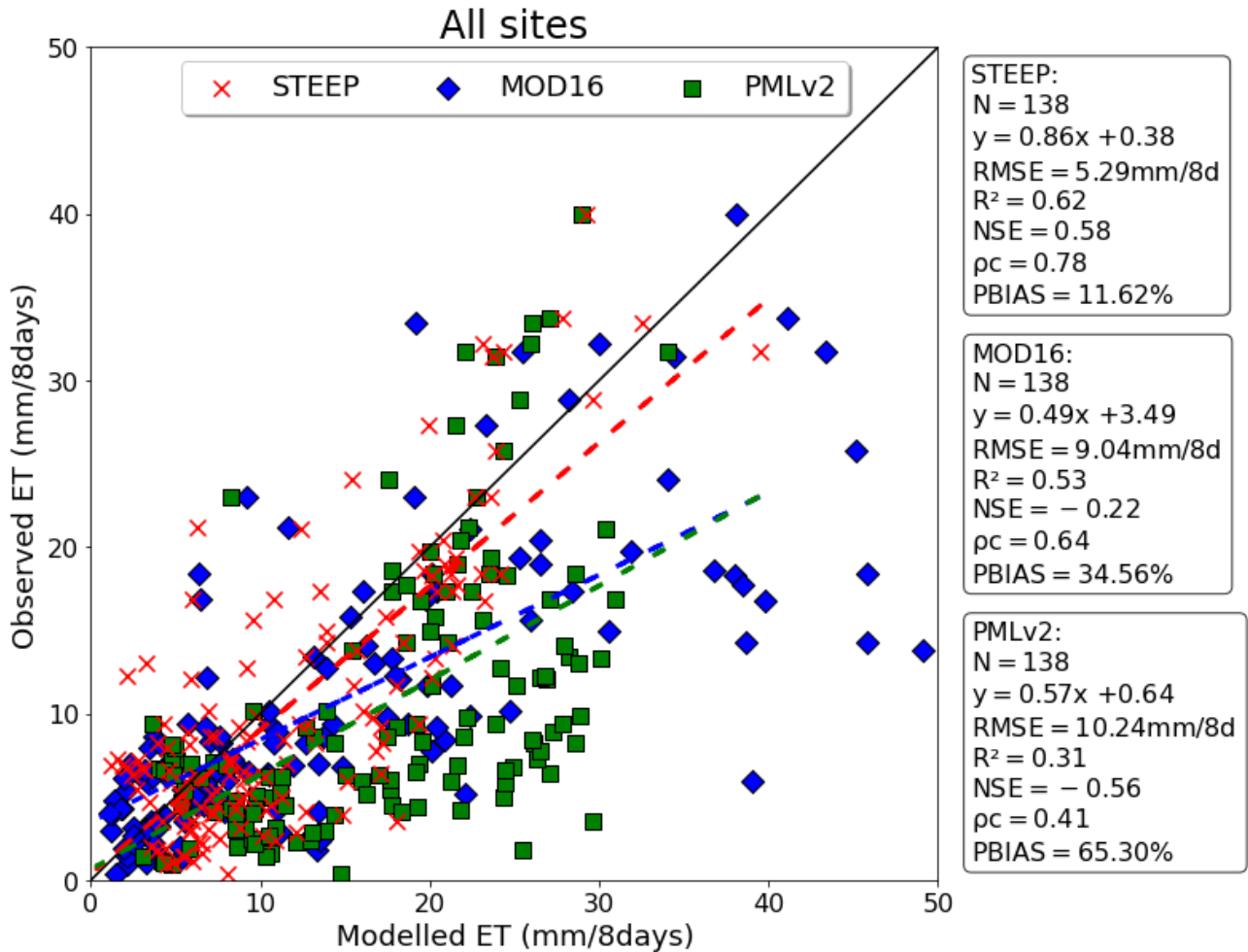
548 The comparison of ET estimates by STEEP, MOD16 and PMLv2 with the observed values  
549 at the different sites (Fig. 8) reveals that the ET estimates by STEEP and global products adequately  
550 followed the seasonality of the values, with a better fit for STEEP and MOD16. In general, the  
551 evaluation at the different sites shows that the *RMSE* of STEEP was not higher than 6.45 mm/8  
552 days, while the ET products' maximum *RMSE* was close to 15 mm/8 days. It is noted that the lowest  
553 *RMSE* value found (4.11 mm/8 days) was for MOD16 at the SET site. Regarding  $R^2$  values, 80% of  
554 the evaluations with STEEP were equal to or greater than 0.50. For MOD16, 60% of the  $R^2$  values  
555 were equal to or greater than 0.70, while for PMLv2, no site had  $R^2$  values that exceeded 0.55. The  
556 best *NSE* value produced by STEEP was 0.77, while with MOD16, it was 0.70, both at the SNN site,  
557 while PMLv2 did not exceed 0.39 (PTN site). Regarding  $\rho_c$ , the percentages of ET evaluations that  
558 obtained values equal to or greater than 0.70 were 60% for STEEP and MOD16, and only 20% for  
559 PMLv2 (site PTN). The overestimations (*PBIAS*) with STEEP were not higher than 50%, and not  
560 higher than 95% with MOD16. For PMLv2 the overestimations did not exceed 80%, except for the  
561 SET site that obtained a *PBIAS* approx. 160%. We highlight the good performance of MOD16 for  
562 the SET, SNN, and especially the PTN sites, with very good performance metrics and seasonal  
563 behaviour, capturing ET values in dry periods very well. The evaluation results of STEEP, MOD16  
564 and PMLv2 for all observation sites combined are shown in Fig. 9. Noteworthy is the better  
565 performance of STEEP over MOD16 and PMLv2, with *RMSE* of < 6 mm/8 days,  $R^2$  and *NSE* greater  
566 than or close to 0.60,  $\rho_c$  of > 0.75 and an average overestimation < 12%. Analysis with the dataset  
567 considering only the 8-day time periods without missing field-observed data, i.e. periods with valid  
568 ET measurements during eight consecutive days (Fig. S3) did not change the results overall,  
569 confirming STEEP's dominance compared to the two standard products evaluated.

570





572 Fig. 8. Temporal evolution of ET from STEEP, MOD16 and PMLv2 for the different observation  
 573 sites, and their individual performance statistics. a), b) and c) PTN 2011; d), e) and f) SNN 2014; g)  
 574 h) and i) SET 2015; j), k) and l) CGR 2014; m), n) and o) CGR 2020. Black lines correspond to  
 575 observed ET while data points refer to estimates by the STEEP model (red crosses), MOD16 (blue  
 576 diamonds) and PMLv2 (green squares) products.



577  
 578 Fig. 9. Evaluation of evapotranspiration (ET, mm/8 days) observed and modelled with STEEP (red  
 579 crosses), MOD16 (blue diamonds) and PMLv2 (green squares) for all experimental sites. The  
 580 black line is the 1:1 line; dashed lines are the fitted linear regressions of observed versus modelled  
 581 values by the STEEP model (red), MOD16 (blue) and PMLv2 (green) products.  $N = 138$  is the total  
 582 number of eight-day periods with at least one day of EC data measured in at least one of the five  
 583 experimental sites of Caatinga where all the ET models (STEEP, MOD16 and PMLv2) outputs  
 584 were available.



585 The explanation of the differences between STEEP and the MOD16 and PMLv2 products is  
586 two-fold. Firstly, the way ET is obtained differs between STEEP and the other products. While  
587 STEEP and other SEB single-source models estimate ET as a combined single process, i.e. soil  
588 evaporation and transpiration estimates are provided as a lumped sum (Sahnoun et al., 2021), and  
589 interception loss is not taken into account, MOD16 and PMLv2 discriminate the ET components, i.e.  
590 soil evaporation, transpiration, and wet canopy evaporation (Mu et al., 2011; Zhang et al., 2019).  
591 With this in mind it is remarkable that STEEP performs better than the other, widely used, multiple-  
592 source ET products. Secondly, the input data sets and their uses are different. The driving  
593 meteorological data for STEEP are from ERA5-Land, while in MOD16, they are from MERRA and in  
594 PMLv2 are provided by GLDAS (Mu et al., 2011; Zhang et al., 2019). In addition, the meteorological  
595 elements used are different among the ET products. MOD16 requires air temperature, atmospheric  
596 pressure, relative humidity, and downward shortwave radiation. In addition to these elements,  
597 PMLv2 also requires precipitation, downward longwave radiation, and wind speed (Mu et al., 2011;  
598 Zhang et al., 2019; Yin et al., 2020; Chen et al., 2022). Although both ET products use the same  
599 land cover data (MOD12Q1), only MOD16 integrates it into its algorithm. In MOD16, the land cover  
600 type defines biome delimitation for the characterization of leaf stomatal conductance, vapour  
601 pressure deficit (VPD) and other related factors, while PMLv2 only uses land cover to construct a  
602 mask of the land area (Chen et al., 2022). The sources and use of LAI in these two products are also  
603 different. LAI is used to increase leaf conductance in MOD16, while it is used to divide the total  
604 available energy into canopy uptake and soil uptake in PMLv2 (Mu et al., 2011; Zhang et al., 2019;  
605 Chen et al., 2022). Although MOD16 uses EC data from 46 distributed sites for validation (Mu et al.,  
606 2011) and PMLv2 uses EC data from 95 distributed sites and ten plant functional types for calibration  
607 (Zhang et al., 2019; Yin et al., 2020), none of the products had observation sites in SDTF.

608 The uncertainties associated with field measurements of ET can also influence the evaluation  
609 of the model products. It is generally accepted that EC flux towers provide reliable local, i.e. for areas  
610 of relatively limited spatial extensions, ca. 10 km<sup>2</sup>, ET measurements (Mu et al., 2011; Chu et al.,  
611 2021; Salazar-Martínez et al., 2022). However, generally flux tower data have a lack of energy  
612 balance closure, that is the difference between net radiation and ground heat flux is sometimes  
613 greater than the sum of the turbulent latent and sensible heat fluxes, an error that can be in the of

614 10–30% range (Wilson et al., 2002; Foken, 2008; Allen et al., 2011). This gap can result from  
615 instrument errors, weather and surface conditions, e.g. those that result in advection, and gap-filling  
616 methods (Mu et al., 2011). In addition, the complex and heterogeneous canopy structure, the  
617 stochastic nature of turbulence (Hollinger and Richardson, 2005) and adverse weather conditions,  
618 e.g. rainy and stormy days, tower sensors recording abnormal values, can affect ET measurements  
619 obtained by EC systems (Ramoelo et al., 2014).

### 620 3.3 Sources of error and further research for STEEP

621 In its current configuration, STEEP has some limitations that should be noted. Meteorological  
622 reanalysis provides only large-scale averages and can misrepresent local meteorological conditions;  
623 hence, it suffers from biases, especially over heterogeneous surfaces (Rasp et al., 2018). However,  
624 despite moderate accuracy and biases at regional scales, ground-based assimilation and reanalysis  
625 data have become important sources of meteorological inputs for ET estimates (Mu et al., 2011;  
626 Zhang et al., 2019; Allam et al., 2021; Senay et al., 2022). Laipelt et al. (2020) and Kayser et al.  
627 (2022) showed that global reanalysis data when used as meteorological inputs had modest effects  
628 only on the accuracy of SEBAL for estimating ET. In our study, ERA5-Land exhibited relatively high  
629 and satisfactory agreement with micrometeorological data measured at each site (Fig. S4). Also,  
630 although gap-filling was used in the present study to improve the availability of LST data, this  
631 procedure should be used with caution. In addition, care should be taken when using the MCD43A4  
632 reflectance product, because in its composition there is also gap-filling. For example, on some cloudy  
633 days, the estimates of vegetation indices, surface albedo, and LST may have introduced  
634 inaccuracies in the STEEP (and in SEBAL) model calculation process due to these gap-filling  
635 methods. Regarding the selection of endmembers pixels, although the temporal evolution of the  
636 selected pixels in this study seems plausible, their representativeness of the actual conditions may  
637 be debatable, especially considering the considerable extent of the AOI. The computational capacity  
638 and the effectiveness of GEE for running SEB models should be commended. Although other studies  
639 have demonstrated GEE's strength (Laipelt et al., 2021; Jaafar et al., 2022; Senay et al., 2022), this  
640 platform has some limitations when it comes to the number of iterations, e.g. a convergence  
641 threshold cannot be set to stop the within-loop iterations of  $H$  calculations; instead a fixed number of

642 iterations needs to be defined. Still, the availability of the several necessary datasets within one  
643 platform greatly facilitates the run of STEEP and other SEB models.

644 One of the main focuses of this study is to provide a one-source model capable of  
645 representing ET in environments that are mainly governed by soil–water availability, such as those  
646 represented by SDTF, in a parsimonious way. Based on our findings we deem this main aim to be  
647 achieved due to the relative simplicity of the STEEP model and its low data demand. The improved  
648 performance of STEEP was the result of improvement of existing and physically meaningful  
649 parameters ( $z_{0m}$  and  $kB^{-1}$ ), rather than by introducing additional empirical parameters, thereby  
650 satisfying the principle of equifinality (see Beven and Freer, 2001). To explore further the potential  
651 and accuracy of STEEP, more research is needed to analyse the impact that the improved  $H$   
652 approach has on ET of different land covers at longer time scales. Despite the promising overall  
653 results, additional efforts are required on modelling  $H$  in SDTF regions. Although we have shown  
654 that STEEP outperforms other models in simulating either  $H$  or ET, we acknowledge that there is still  
655 room for model improvement. Given that the STEEP model was formulated to be a calibration-free  
656 model, it may be possible to improve  $H$  estimates by, for example, optimising coefficients associated  
657 to soil moisture (see Eq A.12) and applying dynamic values to  $q_{pt}$  (see Eq A.25) varying seasonally.  
658 Another potential improvement for instantaneous  $H$  estimates can be achieved by accounting for  
659 biomass heat storage (BHS; Swenson et al., 2019) in STEEP. Meier et al. (2019) have shown that  
660 considering BHS can enable land surface models to capture the diurnal asymmetry of the  
661 temperature impact on energy fluxes and, consequently, provide improved sub-hourly  $H$ . Improving  
662 the quantification of regional ET via RS-based SEB models has a great potential to provide a more  
663 accurate estimate of the energy and water fluxes in SDTF regions, and will contribute to a better  
664 understanding of the water cycle, its uses, and the interrelationships with ecosystem functioning.

#### 665 **4. Conclusions**

666 Our work developed a calibration-free model (STEPP) with an improved approach for  
667 estimating the latent and sensible heat fluxes by remote sensing for SDTF. In summary, the main  
668 conclusions are:

- 669 • The estimates of  $H$  by STEEP allowed ET estimates to be closer to the observed field  
670 values than those obtained by SEBAL. Based on all the performance metrics used to

671 analyse the models, STEEP was superior to SEBAL. STEEP showed *RMSE* less than  
672 1mm/day, *R*<sup>2</sup> between 0.24 and 0.69, *NSE* between -0.17 and 0.65, *ρ*<sub>c</sub> between 0.41  
673 and 0.80 and *PBIAS* between -17% to 54%. Also noteworthy is how well STEEP captured  
674 the seasonal course of observed ET.

675 • Compared with ET data from the global MOD16 and PMLv2 products, the STEEP model  
676 simulated a similar but generally superior seasonal evolution and its performance metrics  
677 were also better. Considering all observation sites simultaneously, at the eight-day scale,  
678 STEEP showed superior performance with *RMSE* less than 6 mm/8 days, *R*<sup>2</sup> and *NSE*  
679 equal to or greater than 0.60, *ρ*<sub>c</sub> greater than 0.75, and an overestimation of < 12%.

680 Thus, we conclude that STEEP, a one-source model that incorporated the seasonality of the  
681 aerodynamic and surface variables, was well-heelled in representing ET in environments that are  
682 mainly governed by soil–water availability. All the same, there is a need to evaluate the newly  
683 developed STEEP model performance for different land covers, climate, and for longer time series  
684 than those considered during the modelling process in this study.

### 685 **Acknowledgements**

686 The Coordenação de Aperfeiçoamento de Pessoal de Nível Superior-Brazil (CAPES)-Finance Code  
687 001, provided scholarships to the first and fifth authors. This work was funded by the Brazilian  
688 National Council for Scientific and Technological Development (CNPq), grant 409341/2021-5, by the  
689 Paraíba Scientific Foundation (FAPESQ), under grants 010/2021 and 403/2021, and by São Paulo  
690 Scientific Foundation (FAPESP), grant 2015/24461-2. CEF is a research unit funded by Fundação  
691 para a Ciência e a Tecnologia I.P. (FCT), Portugal (UIDB/00239/2020). MSBM, AV and RLBN  
692 acknowledge support by the Newton/NERC/FAPESP Nordeste project (NE/N012526/1 ICL 652 and  
693 NE/N012488/1 UoR). RLBN acknowledges support from the European Research Council under the  
694 European Union's Horizon 2020 research and innovation programme (grant agreement No: 787203  
695 REALM). MSBM thanks to Fundação de Amparo à Ciência e Tecnologia do Estado de Pernambuco  
696 (FACEPE) for funding this through the Project FACEPE APQ 0062-1.07/15 (Caatinga-FLUX). MSBM  
697 and AMPM acknowledge to the National Observatory of Water and Carbon Dynamics in the Caatinga  
698 Biome (INCT: NOWCBCB) supported by FACEPE (grant: APQ-0498-3.07/17 ONDACBC), CNPq  
699 (grant: 465764/2014-2), and CAPES (grants: 88887.136369/2017-00).

700 **Data Availability Statement**

701 ET data for the PTN, SNN, and SET sites were published by Melo et al. (2021), and are available at  
702 <https://doi.org/10.5281/zenodo.5549321>. ET data for the CGR site; H data for the PTN, SNN, CGR  
703 sites, and the code used for the formulation of the STEEP model presented in this study can be  
704 accessed at <https://doi.org/10.5281/zenodo.7109043> and  
705 [https://github.com/ulissesaalencar/ET\\_SDTF](https://github.com/ulissesaalencar/ET_SDTF), respectively. H data for the SET site is publicly  
706 available for download at <https://ameriflux.lbl.gov/>.

707 **Supplementary material**

708 Table S1. Performance statistics by the exclusion/modification of one or two parameters/variables  
709 implemented in the STEEP model, in the wet and dry seasons: scale factor soil moisture correction  
710 (SF), the parameter  $kB^{-1}$ , the aerodynamic resistance for heat transfer (rah), PAI replace with LAI  
711 (determined by two different methods), the roughness length for momentum transport ( $z_0m$ ), the  
712 residual latent heat flux in the end members pixels ( $r\lambda ET$ ), and of the SEBAL model.

		Performance statistics									
Site		RMSE		$R^2$		NSE		$\rho_c$		PBIAS	
		wet	dry	wet	dry	wet	dry	wet	dry	wet	dry
PTN (N = 239; 2011)	STEEP	1.23	0.7	0.53	0.62	0.34	0.5	0.68	0.77	-18.01	-17.01
	(-) SF	1.38	0.69	0.56	0.58	0.16	0.52	0.65	0.75	-26.39	-7.99
	(-) kB-1	1.39	0.67	0.54	0.62	0.14	0.55	0.66	0.78	-23.37	-8.23
	(-) rah	1.61	0.66	0.42	0.6	-0.22	0.55	0.54	0.77	-32.42	-6.56
	LAI*	1.37	1.08	0.57	0.59	0.19	-0.18	0.68	0.59	-24.24	-56.26
	LAI**	1.27	0.91	0.54	0.34	0.28	0.17	0.68	0.57	-19.73	-11.95
	(-) z0m	1.48	0.88	0.36	0.3	0.01	0.21	0.5	0.54	-25.94	7.55
	(-) rλET	1.5	1.6	0.12	0.19	-0.15	-1.54	0.31	0.28	14.75	75.96
	(-) z0m & rah	1.51	0.72	0.44	0.51	-0.04	0.48	0.57	0.7	-28.85	4.4
	(-)rah & rλET	1.47	1.66	0.13	0.15	-0.11	-1.81	0.33	0.23	12.99	81.63
	(-) z0m & rλET	1.42	1.45	0.14	0.09	-0.31	-0.04	0.36	0.22	0.73	57.29
	SEBAL	1.39	1.55	0.16	0.12	0.01	-1.43	0.38	0.23	2.12	69.2
	SNN (N = 267; 2014)	STEEP	1.03	0.6	0.46	0.62	0.32	0.25	0.64	0.68	-12.17
(-) SF		1.07	0.58	0.47	0.64	0.29	0.44	0.6	0.73	-17.2	42.77
(-) kB-1		1.12	0.67	0.44	0.59	0.21	0.24	0.6	0.69	-17.86	50.26
(-) rah		1.19	0.6	0.49	0.62	0.19	0.41	0.57	0.7	-25.47	47.33
LAI*		1.38	0.8	0.54	0.3	-0.21	-0.07	0.6	0.44	-29.33	-58.36
LAI**		1.19	0.98	0.52	0.09	0.07	-0.6	0.62	0.26	23.77	55.02
(-) z0m		1.14	0.83	0.41	0.23	0.24	-0.16	0.5	0.37	-19.01	60.45
(-) rλET		1.16	1.18	0.32	0.43	0.18	-1.33	0.51	0.41	12.96	122.85
(-) z0m & rah		1.19	0.63	0.52	0.57	0.17	0.34	0.52	0.64	-26.49	50.69
(-)rah & rλET		1.13	1.14	0.25	0.37	0.16	-1.19	0.47	0.41	6.43	111.65
(-) z0m & rλET		1.13	1.03	0.24	0.17	0.16	-0.79	0.47	0.32	-5.86	79.17
SEBAL		1.13	1.06	0.22	0.33	0.16	-0.88	0.45	0.41	0.91	98.12
SET (N = 283; 2015)		STEEP	1.16	0.6	0.12	0.12	-0.55	-0.94	0.28	0.27	52.19

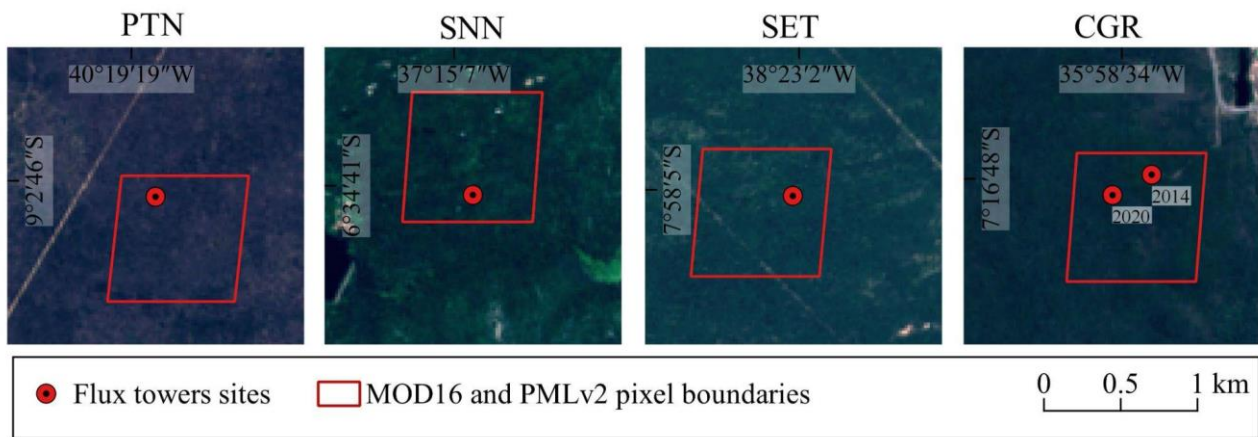
	(-) <i>SF</i>	1.04	0.61	0.11	0.02	-0.25	-0.99	0.28	0.14	36.58	38.26
	(-) <i>kB-1</i>	1.13	0.58	0.06	0.07	-0.49	-0.86	0.21	0.23	36.71	40.83
	(-) <i>rah</i>	1.06	0.56	0.04	0	-0.43	-1.03	0.18	0.03	21.82	39.71
	<i>LAI*</i>	1.3	0.68	0.03	0.09	-0.98	-1.51	0.12	0.2	-62.3	-75.32
	<i>LAI**</i>	1.15	0.6	0.04	0.05	-0.53	-0.97	0.19	0.21	-6.83	-29.78
	(-) <i>z0m</i>	1.09	0.75	0.1	0	-0.36	-2.74	0.26	-0.02	42.62	80.96
	(-) <i>rλET</i>	2.11	1.37	0.15	0.04	-4.18	-9.27	0.15	0.06	151.66	190.07
	(-) <i>z0m &amp; rah</i>	1.06	0.58	0.05	0	-0.3	-1.24	0.21	0.02	21.6	51.96
	(-) <i>rah &amp; rλET</i>	1.99	1.37	0.11	0.01	-3.99	-9.27	0.13	0.04	143.27	183.22
	(-) <i>z0m &amp; rλET</i>	1.66	1.16	0.07	0.01	-2.47	-6.31	0.14	0.04	104.32	134.34
	SEBAL	1.83	1.28	0.1	0	-3.21	-7.93	0.14	0.03	128	161.89
	STEEP	0.8	0.72	0.35	0.51	-0.35	-0.8	0.55	0.58	5.85	25.16
CGR (N = 171; 2014)	(-) <i>SF</i>	0.7	0.67	0.36	0.52	-0.02	-0.53	0.59	0.6	6.57	30.14
	(-) <i>kB-1</i>	0.78	0.8	0.25	0.44	-0.28	-1.18	0.47	0.51	15.04	38.9
	(-) <i>rah</i>	0.71	0.78	0.28	0.46	-0.06	-1.07	0.51	0.48	-8.54	54.63
	<i>LAI*</i>	0.76	0.83	0.49	0.61	-0.23	-1.35	0.64	0.51	-7.64	-62.39
	<i>LAI**</i>	0.75	0.68	0.46	0.58	-0.18	-0.57	0.63	0.63	-9.25	-26.31
	(-) <i>z0m</i>	0.71	0.83	0.28	0.35	-0.05	-1.35	0.51	0.38	-11.12	62.72
	(-) <i>rλET</i>	1.15	2.32	0.09	0.07	-1.77	-17.48	0.19	0.04	46.68	217.84
	(-) <i>z0m &amp; rah</i>	0.69	0.84	0.24	0.44	-0.01	-1.43	0.48	0.39	3.9	68.9
	(-) <i>rah &amp; rλET</i>	1.14	2.44	0.05	0.03	-1.72	-19.4	0.15	0.02	43.77	229.58
	(-) <i>z0m &amp; rλET</i>	0.85	1.97	0.11	0.04	-0.51	-12.27	0.33	0.04	9.18	175.39
	SEBAL	0.97	2.24	0.07	0.03	-0.97	-14.7	0.21	0.03	28.63	208.13
	STEEP	0.61	1.06	0.39	0.02	0.29	-2.98	0.62	0.09	-1.19	101.37
CGR (N = 48; 2020)	(-) <i>SF</i>	0.82	1.03	0.3	0	-0.29	-2.76	0.52	0.02	-6.52	106.36
	(-) <i>kB-1</i>	0.83	1.26	0.29	0	-0.3	-4.63	0.51	-0.03	-5.31	135.98
	(-) <i>rah</i>	1.11	1.13	0.25	0	-1.2	-3.55	0.42	-0.02	-15.37	133.29
	<i>LAI*</i>	0.85	1.02	0.29	0.01	-0.38	-0.99	-3.06	0.4	-4.71	31.63
	<i>LAI**</i>	0.67	0.76	0.36	0.07	0.14	-1.03	0.59	0.26	-3.58	2.87

(-) $z0m$	0.69	1.03	0.41	0	0.15	-2.73	0.58	-0.02	-12.29	106.1
(-) $r\lambda ET$	0.99	2.25	0.03	0.06	-0.52	-16.98	0.17	-0.04	6.37	312.54
(-) $z0m$ & $rah$	1.04	1.13	0.34	0.01	-0.74	-3.52	0.5	-0.03	-16.56	134.92
(-) $rah$ & $r\lambda ET$	0.89	2.38	0.05	0.14	-0.24	-19.08	0.22	-0.05	1.07	330.94
(-) $z0m$ & $r\lambda ET$	0.83	1.77	0.18	0.02	-0.6	-10.14	0.33	-0.04	-14.15	216.81
SEBAL	0.81	2.11	0.16	0.07	-0.02	-0.02	0.31	-0.04	-12.25	285.53

714

715  $z0m$  = roughness length for momentum transfer;  $rah$  = aerodynamic resistance for heat transfer;  $r\lambda ET$  = remaining  $\lambda ET$  in the endmembers pixels.



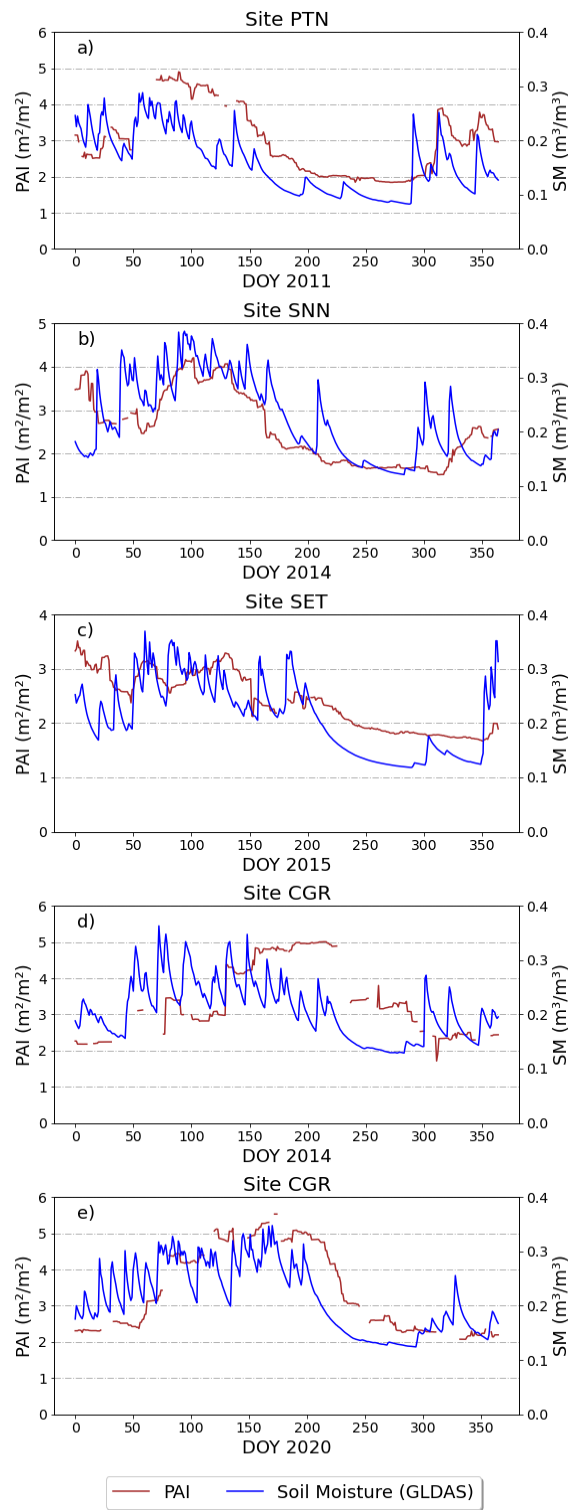


716

717 Fig. S1. Location of the flux towers sites and MOD16 and PMLv2 pixel boundaries. True colour  
 718 composite (bands 4, 3, and 2) of Harmonized Sentinel-2 MSI acquired via Google Earth Engine.

719 Scene acquired of PTN (12/06/2021); SNN and SET (25/05/2021); CGR (29/07/2021).

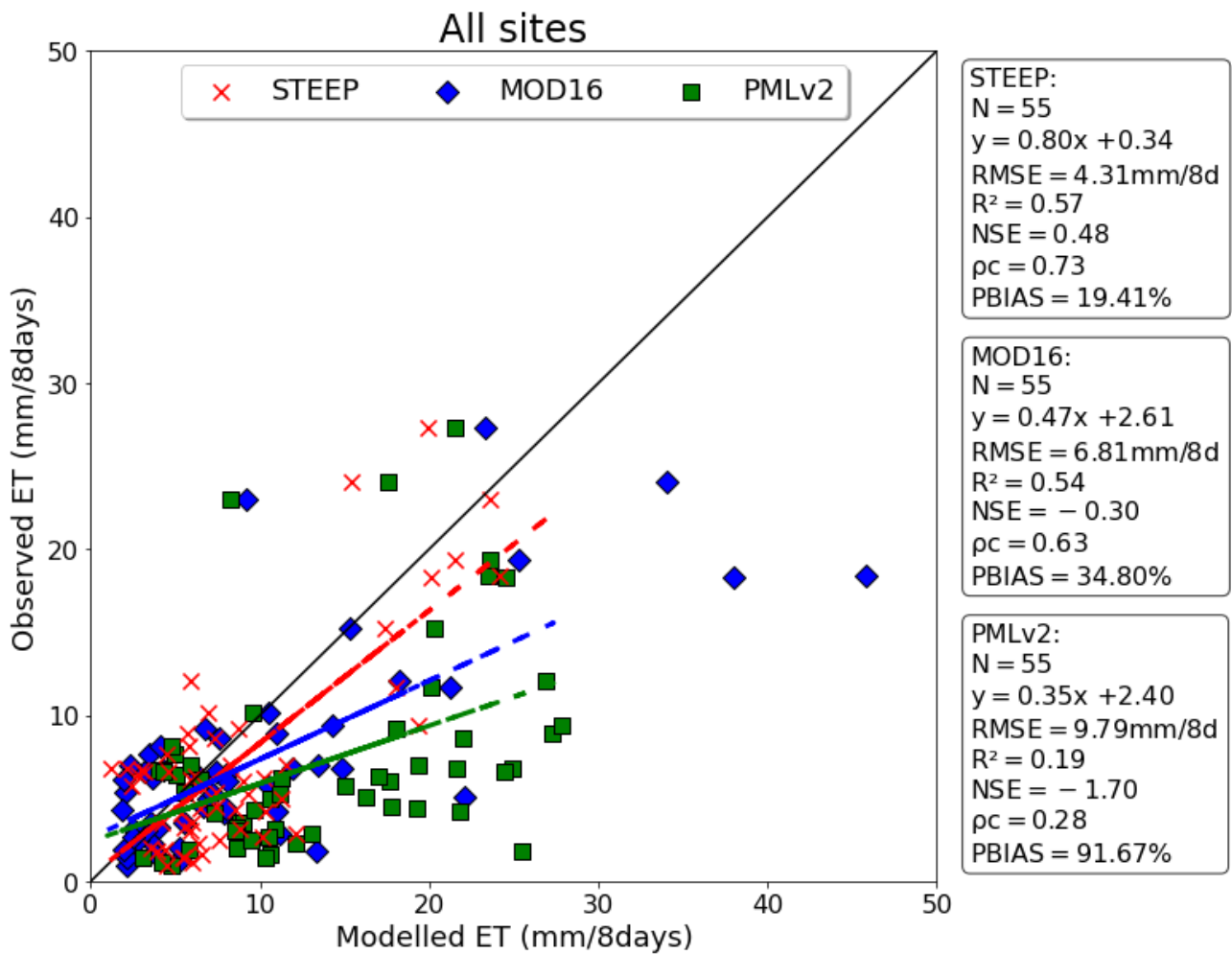
720



721

722

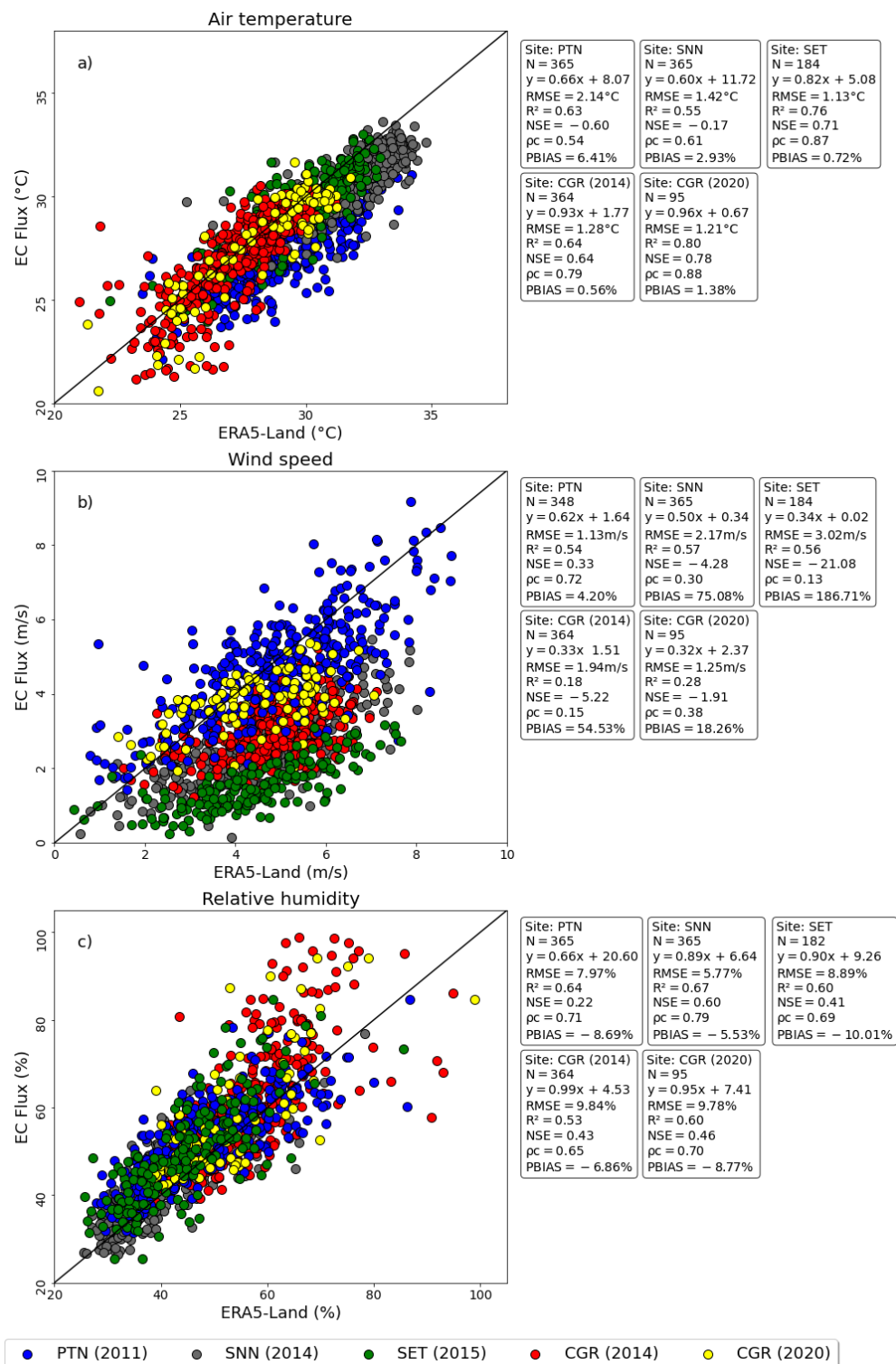
Fig. S2. PAI and soil moisture time series for the different observation sites.



723

724 Fig. S3. Evaluation of evapotranspiration (ET, mm/8 days) observed and modelled with STEEP  
 725 (red crosses), MOD16 (blue diamonds) and PMLv2 (green squares) for all experimental sites  
 726 considering only the 55 periods where the field-observed data had eight consecutive days. The  
 727 black line is the 1:1 line; dashed lines are the fitted linear regressions of observed or modelled  
 728 values by the STEEP model (red), MOD16 (blue) and PMLv2 (green) products.

729



730

731

732

733

734

735

736

Fig. S4. Comparison between ERA5-Land reanalysis dataset and local observational meteorological measurements from the flux tower at the closest time from the satellite overpass. Micrometeorological sensors installed at the flux towers are up to 16 m in distance from the land surface, and ERA5-Land variables have different reference elevation (e.g. 2 m for air temperature and 10 m to wind speed).

737 **Appendix A – Equations adopted to formulate the STEEP model**

738 Latent heat flux ( $\lambda ET$ ) was modeled using Eq. (A.1):

$$\lambda ET = R_n - G - H \quad (\text{A.1})$$

739 where  $R_n$  is net radiation,  $G$  is soil heat flux, and  $H$  is sensible heat flux. All variables are expressed  
740 in energy units (e.g.,  $\text{W/m}^2$ ).

741 Net radiation ( $R_n$ ) was modeled based on the radiation budget indicated by Allen et al. (2007) and  
742 Ferreira et al. (2020) by Eq. (A.2):

$$R_n = R_{S\downarrow} \times (1 - \alpha) + \varepsilon_s \times R_{L\downarrow} - R_{L\uparrow} \quad (\text{A.2})$$

743 where  $R_{S\downarrow}$  is incident shortwave radiation ( $\text{W/m}^2$ ) estimated following Allen et al. (2007),  $\alpha$  is surface  
744 albedo (dimensionless), estimated following Trezza et al. (2013),  $R_{L\downarrow}$  is longwave radiation from the  
745 atmosphere ( $\text{W/m}^2$ ) estimated following Ferreira et al. (2020) with atmospheric emissivity from  
746 Duarte et al. (2006);  $R_{L\uparrow}$  is emitted longwave radiation ( $\text{W/m}^2$ ) following Ferreira et al. (2020) with  $\varepsilon_s$   
747 the surface emissivity (dimensionless), estimated following Long et al. (2010).

748 Soil heat flux ( $G$ ), expressed as a ratio of net radiation, was estimated following the model by  
749 Bastiaanssen et al. (1998):

$$\frac{G}{R_n} = [(LST - 273.15) \times (0.0038 + 0.0074 \times \alpha) \times (1 - 0.98 \times NDVI^4)] \quad (\text{A.3})$$

750 where  $LST$  is the surface temperature (K) and NDVI is the Normalized Difference Vegetation Index  
751 (dimensionless), estimated following Rouse et al. (1973).

752 Sensible heat flux ( $H$ ) was modeled using:

$$H = \frac{\rho \times c_p \times dT}{rah} \quad (\text{A.4})$$

753 where  $\rho$  is the air density ( $\text{kg/m}^3$ ),  $c_p$  refers to the specific heat of air at constant pressure ( $\text{J/kg/K}$ ),  
754  $dT$  is the temperature gradient (K), and  $rah$  is the aerodynamic resistance for heat transfer (s/m).

755

756 Aerodynamic resistance to heat transport was estimated based on the classical equation given in  
757 Paul et al. (2013), see also Verhoef et al. (1997a):

$$rah = \frac{1}{k \times u^*} \times \left[ \ln \left( \frac{z_{ref} - d0}{z0m} \right) - \psi_h \right] + \frac{1}{k \times u^*} \times kB_{umd}^{-1} \quad (A.5)$$

758 where  $k$  is the von Kármán constant taken as 0.41,  $u^*$  is the friction velocity (m/s),  $z_{ref}$  is the  
 759 reference height (m),  $d0$  is zero plane displacement height (m),  $z0m$  is roughness length for  
 760 momentum transfer (m),  $\psi_h$  is the atmospheric stability correction function for heat transfer (m), as  
 761 calculated following Paulson (1970),  $kB_{umd}^{-1}$  is the dimensionless parameter formulated to express  
 762 the excess resistance of heat transfer compared to momentum transfer, corrected for soil moisture  
 763 derived from remote sensing.

764 The friction velocity was computed according to Verhoef et al. (1997b) and Paul et al. (2013):

$$u^* = k \times u \left[ \ln \left( \frac{z_{ref} - d0}{z0m} \right) - \psi_m \right]^{-1} \quad (A.6)$$

765 where  $u$  is the wind speed (m/s) at a known height  $z_{ref}$ ,  $\psi_m$  is the atmospheric stability correction  
 766 function for momentum transfer (m), as calculated following Paulson (1970).

767 Roughness length for momentum transport was estimated, based on the studies by Verhoef et al.  
 768 (1997b):

$$z0m = (HGHT - d0) \times \exp(-k \times \gamma + PSICORR) \quad (A.7)$$

769 where  $HGHT$  is the height of the vegetation (m),  $PSICORR$  is taken as 0.2 and  $\gamma$  is the inverse of the  
 770 square root of the bulk surface drag coefficient at the roughness canopy height (Raupach, 1992).

771 Zero plane displacement height ( $d0$ ) was obtained following Raupach (1994) from:

$$d0 = HGHT \times \left[ \left( 1 - \frac{1}{\sqrt{CD1 \times PAI}} \right) + \left( \frac{\exp^{-\sqrt{CD1 \times PAI}}}{\sqrt{CD1 \times PAI}} \right) \right] \quad (A.8)$$

772 where  $CD1$  is taken as 20.6 and  $PAI$  is the Plant Area Index.

773  $\gamma$  was following Verhoef et al. (1997b):

$$\gamma = \left( CD + CR \times \frac{PAI}{2} \right)^{-0.5} \quad (A.9)$$

774 if  $\gamma < 3.33$ ,  $\gamma$  is set to 3.33. Following Verhoef et al. (1997),  $CD$  and  $CR$  are taken as 0.01 and 0.35,  
 775 respectively.

776 Plant Area Index was calculated according to Miranda et al. (2020) as:

$$PAI = 10.1 \times (\rho_{NIR} - \sqrt{\rho_{RED}}) + 3.1 \quad (A.10)$$

777 where  $\rho_{NIR}$  is the near infrared band reflectance, and  $\rho_{RED}$  is the red band reflectance. If  $PAI < 0$ ,  $d0$   
 778 is set to 0.

779 The dimensionless parameter  $kB_{umd}^{-1}$  is corrected by soil moisture by remote sensing following the  
 780 equations provided by Gokmen et al. (2012):

$$kB_{umd}^{-1} = SF \times kB^{-1} \quad (A.11)$$

781 where  $SF$  is a scaling factor, represented by a sigmoid function:

$$SF = \left[ c + \frac{1}{1 + \exp(d - e \times SM_{rel})} \right] \quad (A.12)$$

782 Here,  $c$ ,  $d$ ,  $e$  are the sigmoid function coefficients, for which we adopted values of 0.3, 2.5, and 4,  
 783 respectively, following Gokmen et al. (2012).  $SM_{rel}$  is the relative soil moisture, obtained from:

$$SM_{rel} = \frac{SM - SM_{min}}{SM_{max} - SM_{min}} \quad (A.13)$$

784 where  $SM$  is the actual soil moisture content, in our case obtained with the GLDAS reanalysis  
 785 product, and  $SM_{min}$  and  $SM_{max}$  are the minimum and maximum soil moisture. The  $SM_{min}$  and  $SM_{max}$   
 786 values were obtained using the annual time series analysis of the soil moisture data.

787  $kB^{-1}$  was calculated according to Su et al. (2001):

$$kB^{-1} = \frac{k \times Cd}{4 \times Ct \times \frac{u^*}{u(h)} \times \left( 1 - \exp\left(\frac{-nec}{2}\right) \right)} \times f_c^2 + \frac{k \times \frac{u^*}{u(h)} \times \frac{z0m}{h}}{C_t^*} \times f_c^2 \times f_s^2 + kB_s^{-1} \times f_s^2 \quad (A.14)$$

788 where  $kB_s^{-1} = 2.46(Re^*)^{0.25} - 2$ ,  $Cd$  is the drag coefficient of the foliage elements taken as 0.2,  $Ct$   
 789 is the heat transfer coefficient of the leaf with value 0.01.

790 The ratio  $\frac{u^*}{u(h)}$  is parameterized as:

$$\frac{u^*}{u(h)} = c1 - c2 \times \exp(-c3 \times Cd \times PAI) \quad (A.15)$$

791 where  $c1 = 0.320$ ,  $c2 = 0.264$ ,  $c3 = 15.1$ .

792  $nec$  is the extinction coefficient of the wind speed profile within the canopy given by:

$$nec = \frac{Cd \times PAI}{\frac{2u^{*2}}{u(h)^2}} \quad (A.16)$$

793  $C_t^*$  is heat transfer coefficient of the soil given by:

$$C_t^* = Pr^{-2/3} \times (Re)^{-1/2} \quad (A.17)$$

794 where  $Pr$  is the Prandtl number with a value 0.71, and  $Re$  is the Reynolds number calculated as:

$$Re = \frac{u^* \times 0.009}{\nu}, \quad \nu = 1.461 \times 10^{-5} \quad (A.18)$$

795 where  $\nu$  is the kinematic viscosity (m<sup>2</sup>/s).

796 In Eq. A.14  $f_c$  is the fractional canopy cover calculated according to Eq. (A19), and  $f_s$  is its  
797 complement.

$$f_c = 1 - \left[ \frac{NDVI - NDVI_{max}}{NDVI_{min} - NDVI_{max}} \right]^{0.4631} \quad (A.19)$$

798 where  $NDVI_{max}$  and  $NDVI_{min}$  are maximum and minimum NDVI values, respectively.  $NDVI_{max}$  and  
799  $NDVI_{min}$  values were obtained using the annual time series analysis of the NDVI.

800  $dT$  in Eq. (A4) was estimated daily with a linear relationship on the surface temperature  
801 (Bastiaanssen et al., 1998) as:

$$dT = a + b \times LST \quad (A.20)$$

802 To find the coefficients  $a$  and  $b$  in Eq. (A20) requires that hot and cold endmembers pixels are  
803 established. The coefficients were found as:

$$b = \frac{(dT_{hot} - dT_{cold})}{(LST_{hot} - LST_{cold})} \quad (A.21)$$

$$a = dT_{cold} - b \times LST_{cold} \quad (A.22)$$

$$dT_{hot/cold} = \frac{H_{hot/cold} \times rah_{hot/cold}}{\rho \times c_p} \quad (A.23)$$

$$H_{hot/cold} = Rn_{hot/cold} - G_{hot/cold} - \lambda ET_{hot/cold} \quad (A.24)$$



804 where  $dT_{hot/cold}$  are  $dT$  values for the hot/dry and cold/wet endmember pixels, respectively,  
 805  $Rn_{hot/cold}$ ,  $G_{hot/cold}$ ,  $LST_{hot/cold}$ ,  $rah_{hot/cold}$  are the median values extracted on the endmember  
 806 pixels of each variable. The selection of endmember pixels is detailed in section 2.3.

807  $\lambda ET_{hot/cold}$  is the term incorporated in the computation of  $H$  in the endmember pixels given by the  
 808 Priestley-Taylor (1972) equation, according to Singh and Irmak (2011) and French et al. (2015):

$$\lambda ET_{hot/cold} = (Rn_{hot/cold} - G_{hot/cold}) \times f_c \times \alpha_{pt} \times \left[ \frac{\Delta}{\Delta + \gamma_c} \right] \quad (A.25)$$

809 where  $\alpha_{pt}$  is the empirical Priestley-Taylor coefficient, nominally set to 1.26, but here adjusted  
 810 according to local conditions, i.e. we adopted the  $\alpha_{pt}$  values (0.55 for hot/dry and 1.75 for cold/wet  
 811 pixels) based on Ai and Yang (2016).  $\Delta$  is the slope of the saturation vapor pressure-air temperature  
 812 curve (kPa/°C) and  $\gamma_c$  is the psychrometric constant (kPa/°C).

813 The actual daily evapotranspiration (mm/day) was obtained by means of the following relationship:

$$ET_{24h} = \frac{86400}{(2.501 - 0.00236 \times T_a) \times 10^6} \times \frac{\lambda ET}{Rn - G} \times Rn_{24h} \quad (A.26)$$

814 where  $T_a$  is the mean daily air temperature (°C),  $\lambda ET$  is derived from Eq. A1, and  $Rn_{24h}$  corresponds  
 815 to the daily net radiation (W/m<sup>2</sup>); in this study both driving variables were obtained with data from the  
 816 ERA5-Land product.

## 817 **References**

- 818 Ai, Z., & Yang, Y. (2016). Modification and Validation of Priestley–Taylor Model for Estimating Cotton  
 819 Evapotranspiration under Plastic Mulch Condition. *Journal of Hydrometeorology*, 17(4), 1281–1293.  
 820 doi:10.1175/jhm-d-15-0151.1
- 821 Akoglu, H. (2018). User's guide to correlation coefficients. *Turkish Journal of Emergency Medicine*,  
 822 18(3), 91-93. doi: 10.1016/j.tjem.2018.08.001
- 823 Alberton, B., Torres, R. da S., Cancian, L. F., Borges, B. D., Almeida, J., Mariano, G. C., ... Morellato,  
 824 L. P. C. (2017). Introducing digital cameras to monitor plant phenology in the tropics: applications for  
 825 conservation. *Perspectives in Ecology and Conservation*, 15(2), 82–90.  
 826 doi:10.1016/j.pecon.2017.06.004

827 Allam, M., Mhaweji, M., Meng, Q., Faour, G., Abunnasr, Y., Fadel, A., & Xinli, H. (2021). Monthly 10-  
828 m evapotranspiration rates retrieved by SEBALI with Sentinel-2 and MODIS LST data. *Agricultural*  
829 *Water Management*, 243, 106432. doi:10.1016/j.agwat.2020.106432

830 Allen, R. G., Tasumi, M., & Trezza, R. (2007). Satellite-Based Energy Balance for Mapping  
831 Evapotranspiration with Internalized Calibration (METRIC)—Model. *Journal of Irrigation and*  
832 *Drainage Engineering*, 133(4), 380–394. doi:10.1061/(asce)0733-9437(2007)133:4(380)

833 Allen, K., Dupuy, J. M., Gei, M. G., Hulshof, C., Medvigy, D., Pizano, C., ... Powers, J. S. (2017).  
834 Will seasonally dry tropical forests be sensitive or resistant to future changes in rainfall regimes?  
835 *Environmental Research Letters*, 12(2), 023001. doi:10.1088/1748-9326/aa5968

836 Allen, R. G., Pereira, L. S., Howell, T. A., & Jensen, M. E. (2011). Evapotranspiration information  
837 reporting: I. Factors governing measurement accuracy. *Agricultural Water Management*, 98(6), 899–  
838 920. doi:10.1016/j.agwat.2010.12.015

839 Alvares, C. A., Stape, J. L., Sentelhas, P. C., Gonçalves, J. D. M., & Sparovek, G. (2013). Köppen's  
840 climate classification map for Brazil. *Meteorologische Zeitschrift*, 22(6), 711-728. doi:10.1127/0941-  
841 2948/2013/0507

842 Anapalli, S. S., Ahuja, L. R., Gowda, P. H., Ma, L., Marek, G., Evett, S. R., & Howell, T. A. (2016).  
843 Simulation of crop evapotranspiration and crop coefficients with data in weighing lysimeters.  
844 *Agricultural Water Management*, 177, 274–283. doi:10.1016/j.agwat.2016.08.009

845 Anderson, M. C., Kustas, W. P., Norman, J. M., Hain, C. R., Mecikalski, J. R., Schultz, L., ... Gao,  
846 F. (2011). Mapping daily evapotranspiration at field to continental scales using geostationary and  
847 polar orbiting satellite imagery. *Hydrology and Earth System Sciences*, 15(1), 223–239.  
848 doi:10.5194/hess-15-223-2011

849 Andrade, J., Cunha, J., Silva, J., Rufino, I., & Galvão, C. (2021). Evaluating single and multi-date  
850 Landsat classifications of land-cover in a seasonally dry tropical forest. *Remote Sensing*  
851 *Applications: Society and Environment*, 22, 100515. doi:10.1016/j.rsase.2021.100515

852 Antonino, A. C. D. (2019), AmeriFlux BASE BR-CST Caatinga Serra Talhada, Ver. 1-5, AmeriFlux  
853 AMP, (Dataset). <https://doi.org/10.17190/AMF/1562386>

854 Araújo, J. C., & González Piedra, J. I. (2009). Comparative hydrology: analysis of a semiarid and a  
855 humid tropical watershed. *Hydrological Processes*, 23(8), 1169–1178. doi:10.1002/hyp.7232

856 Barbosa, H. A., Huete, A. R., & Baethgen, W. E. (2006). A 20-year study of NDVI variability over the  
857 Northeast Region of Brazil. *Journal of Arid Environments*, 67(2), 288–307.  
858 doi:10.1016/j.jaridenv.2006.02.022

859 Barbosa, A. D. S., Andrade, A. P. de, Félix, L. P., Aquino, Í. D. S., & Silva, J. H. C. S. (2020).  
860 Composição, similaridade e estrutura do componente arbustivo-arbóreo de áreas de Caatinga.  
861 *Nativa*, 8(3), 314–322. doi:10.31413/nativa.v8i3.9494

862 Barraza, V., Restrepo-Coupe, N., Huete, A., Grings, F., Beringer, J., Cleverly, J., & Eamus, D.  
863 (2017). Estimation of latent heat flux over savannah vegetation across the North Australian Tropical  
864 Transect from multiple sensors and global meteorological data. *Agricultural and Forest Meteorology*,  
865 232, 689-703. doi:10.1016/j.agrformet.2016.10.013

866 Bastiaanssen, W. G. M. (1995). Regionalization of surface flux densities and moisture indicators in  
867 composite terrain: A remote sensing approach under clear skies in Mediterranean climates.  
868 Wageningen University and Research.

869 Bastiaanssen, W. G. M., Menenti, M., Feddes, R. A., & Holtslag, A. A. M. (1998). A remote sensing  
870 surface energy balance algorithm for land (SEBAL). 1. Formulation. *Journal of Hydrology*, 212-213,  
871 198–212. doi:10.1016/s0022-1694(98)00253-4

872 Bastiaanssen, W. G. M., Ahmad, M.-D., & Chemin, Y. (2002). Satellite surveillance of evaporative  
873 depletion across the Indus Basin. *Water Resources Research*, 38(12), 9–1–9–9.  
874 doi:10.1029/2001wr000386

875 Bastiaanssen, W. G. M., Noordman, E. J. M., Pelgrum, H., Davids, G., Thoreson, B. P., & Allen, R.  
876 G. (2005). SEBAL Model with remotely sensed data to improve water-resources management under

877 actual field conditions. *Journal of Irrigation and Drainage Engineering*, 131(1), 85–93.  
878 doi:10.1061/(asce)0733-9437(2005)131:1(85)

879 Beven, K., & Freer, J. (2001). Equifinality, data assimilation, and uncertainty estimation in  
880 mechanistic modelling of complex environmental systems using the GLUE methodology. *Journal of*  
881 *Hydrology*, 249(1–4), 11–29. doi:10.1016/s0022-1694(01)00421-8

882 Bhattarai, N., Quackenbush, L. J., Im, J., & Shaw, S. B. (2017). A new optimized algorithm for  
883 automating endmember pixel selection in the SEBAL and METRIC models. *Remote Sensing of*  
884 *Environment*, 196, 178–192. doi:10.1016/j.rse.2017.05.009.

885 Bonan, G. B., Patton, E. G., Finnigan, J. J., Baldocchi, D. D., & Harman, I. N. (2021). Moving beyond  
886 the incorrect but useful paradigm: reevaluating big-leaf and multilayer plant canopies to model  
887 biosphere-atmosphere fluxes – a review. *Agricultural and Forest Meteorology*, 306, 108435.  
888 <https://doi.org/10.1016/j.agrformet.2021.108435>

889 Borges, C. K., dos Santos, C. A. C., Carneiro, R. G., da Silva, L. L., de Oliveira, G., Mariano, D., ...  
890 de S. Medeiros, S. (2020). Seasonal variation of surface radiation and energy balances over two  
891 contrasting areas of the seasonally dry tropical forest (Caatinga) in the Brazilian semi-arid.  
892 *Environmental Monitoring and Assessment*, 192(8). doi:10.1007/s10661-020-08484-y

893 Brazil, Ministério do Meio Ambiente. Caatinga. <https://antigo.mma.gov.br/biomas/caatinga.html>.  
894 Accessed: 25 March 2021.

895 Cabral, O. M. R., Freitas, H. C., Cuadra, S. V., de Andrade, C. A., Ramos, N. P., Grutzmacher, P.,  
896 ... Rossi, P. (2020). The sustainability of a sugarcane plantation in Brazil assessed by the eddy  
897 covariance fluxes of greenhouse gases. *Agricultural and Forest Meteorology*, 282-283, 107864.  
898 doi:10.1016/j.agrformet.2019.107864

899 Campos, S., Mendes, K. R., da Silva, L. L., Mutti, P. R., Medeiros, S. S., Amorim, L. B., ... Bezerra,  
900 B. G. (2019). Closure and partitioning of the energy balance in a preserved area of a Brazilian

901 seasonally dry tropical forest. *Agricultural and Forest Meteorology*, 271, 398–412.  
902 doi:10.1016/j.agrformet.2019.03.018

903 Carvalho, H. F. D. S., de Moura, M. S., da Silva, T. G., & Rodrigues, C. T. (2018). Controlling factors  
904 of 'Caatinga' and sugarcane evapotranspiration in the Sub-middle São Francisco Valley. *Revista*  
905 *Brasileira de Engenharia Agrícola e Ambiental*, 22, 225-230. doi:10.1590/1807-  
906 1929/agriambi.v22n4p225-230

907 Chai, T., & Draxler, R. R. (2014). Root mean square error (RMSE) or mean absolute error (MAE)?  
908 – Arguments against avoiding RMSE in the literature. *Geoscientific Model Development*, 7(3), 1247–  
909 1250. doi:10.5194/gmd-7-1247-2014

910 Chehbouni, A., Seen, D. L., Njoku, E. G., & Monteny, B. M. (1996). Examination of the difference  
911 between radiative and aerodynamic surface temperatures over sparsely vegetated surfaces. *Remote*  
912 *Sensing of Environment*, 58(2), 177-186. doi: 10.1016/S0034-4257(96)00037-5

913 Chen, J. M., & Liu, J. (2020). Evolution of evapotranspiration models using thermal and shortwave  
914 remote sensing data. *Remote Sensing of Environment*, 237, 111594. doi:10.1016/j.rse.2019.111594

915 Chen, H., Gnanamoorthy, P., Chen, Y., Mansaray, L. R., Song, Q., Liao, K., ... Sun, C. (2022).  
916 Assessment and Inter-Comparison of Multi-Source High Spatial Resolution Evapotranspiration  
917 Products over Lancang–Mekong River Basin, Southeast Asia. *Remote Sensing*, 14(3), 479.  
918 doi:10.3390/rs14030479

919 Cheng, M., Jiao, X., Li, B., Yu, X., Shao, M., & Jin, X. (2021). Long time series of daily  
920 evapotranspiration in China based on the SEBAL model and multisource images and validation.  
921 *Earth System Science Data*, 13(8), 3995–4017. doi:10.5194/essd-13-3995-2021

922 Chu, H., et al. (2021) Representativeness of Eddy-Covariance flux footprints for areas surrounding  
923 AmeriFlux sites." *Agricultural and Forest Meteorology* 301-302, 108350.  
924 doi:org/10.1016/j.agrformet.2021.108350

925 Costa, J. A.; Navarro-Hevia, J., Costa, C. A. G., & de Araújo, J. C. (2021). Temporal dynamics of  
926 evapotranspiration in semiarid native forests in Brazil and Spain using remote sensing. *Hydrological*  
927 *Processes*, 35(3). doi:10.1002/hyp.14070

928 Costa-Filho, E., Chávez, J. L., Zhang, H., & Andales, A. A. (2021). An optimized surface aerodynamic  
929 temperature approach to estimate maize sensible heat flux and evapotranspiration. *Agricultural and*  
930 *Forest Meteorology*, 311, 108683. doi:10.1016/j.agrformet.2021.108683

931 Cunha, J., Nóbrega, R. L. B., Rufino, I., Erasmi, S., Galvão, C., & Valente, F. (2020). Surface albedo  
932 as a proxy for land-cover clearing in seasonally dry forests: Evidence from the Brazilian Caatinga.  
933 *Remote Sensing of Environment*, 238, 111250. doi:10.1016/j.rse.2019.111250

934 Danelichen, V. H. de M., Biudes, M. S., Souza, M. C., Machado, N. G., Silva, B. B. da, & Nogueira,  
935 J. de S. (2014). Estimation of soil heat flux in a neotropical Wetland region using remote sensing  
936 techniques. *Revista Brasileira de Meteorologia*, 29(4), 469–482. doi:10.1590/0102-778620120568

937 Dombroski, J. L. D., Praxedes, S. C., de Freitas, R. M. O., & Pontes, F. M. (2011). Water relations  
938 of Caatinga trees in the dry season. *South African Journal of Botany*, 77(2), 430–434.  
939 doi:10.1016/j.sajb.2010.11.001

940 Duarte, H. F., Dias, N. L., & Maggiotto, S. R. (2006). Assessing daytime downward longwave  
941 radiation estimates for clear and cloudy skies in Southern Brazil. *Agricultural and Forest*  
942 *Meteorology*, 139(3–4), 171–181. doi:10.1016/j.agrformet.2006.06.008

943 Faivre, R., Colin, J., & Menenti, M. (2017). Evaluation of Methods for Aerodynamic Roughness  
944 Length Retrieval from Very High-Resolution Imaging LIDAR Observations over the Heihe Basin in  
945 China. *Remote Sensing*, 9(1), 63. doi:10.3390/rs9010063

946 Farr, T. G., Rosen, P. A., Caro, E., Crippen, R., Duren, R., Hensley, S., ... & Alsdorf, D. (2007). The  
947 shuttle radar topography mission. *Reviews of geophysics*, 45(2). doi:10.1029/2005RG000183

948 Ferreira, T. R., Silva, B. B. D., Moura, M. S. B. D., Verhoef, A., & Nóbrega, R. L. B. (2020). The use  
949 of remote sensing for reliable estimation of net radiation and its components: a case study for

950 contrasting land covers in an agricultural hotspot of the Brazilian semiarid region. *Agricultural and*  
951 *Forest Meteorology*, 291, 108052. doi:10.1016/j.agrformet.2020.108052

952 Foken, T. (2008). The energy balance closure problem: An overview. *Ecological Applications*, 18(6),  
953 1351-1367. doi:10.1890/06-0922.1

954 French, A. N., Hunsaker, D. J., & Thorp, K. R. (2015). Remote sensing of evapotranspiration over  
955 cotton using the TSEB and METRIC energy balance models. *Remote Sensing of Environment*, 158,  
956 281–294. doi:10.1016/j.rse.2014.11.003

957 Funk, C., Peterson, P., Landsfeld, M., Pedreros, D., Verdin, J., Shukla, S., ... & Michaelsen, J. (2015).  
958 The climate hazards infrared precipitation with stations—a new environmental record for monitoring  
959 extremes. *Scientific data*, 2(1), 1-21. doi:10.1038/sdata.2015.66

960 Gan, R., Zhang, Y., Shi, H., Yang, Y., Eamus, D., Cheng, L., ... Yu, Q. (2018). Use of satellite leaf  
961 area index estimating evapotranspiration and gross assimilation for Australian ecosystems.  
962 *Ecohydrology*, 11(5), e1974. doi:10.1002/eco.1974

963 Gokmen, M., Vekerdy, Z., Verhoef, A., Verhoef, W., Batelaan, O., & van der Tol, C. (2012).  
964 Integration of soil moisture in SEBS for improving evapotranspiration estimation under water stress  
965 conditions. *Remote Sensing of Environment*, 121, 261–274. doi:10.1016/j.rse.2012.02.003

966 Gorelick, N., Hancher, M., Dixon, M., Ilyushchenko, S., Thau, D., & Moore, R. (2017). Google Earth  
967 Engine: Planetary-scale geospatial analysis for everyone. *Remote Sensing of Environment*, 202,  
968 18–27. doi:10.1016/j.rse.2017.06.031

969 Gupta, H. V., Sorooshian, S., & Yapo, P. O. (1999). Status of automatic calibration for hydrologic  
970 models: Comparison with multilevel expert calibration. *Journal of hydrologic engineering*, 4(2), 135-  
971 143. doi:10.1061/(ASCE)1084-0699(1999)4:2(135)

972 Hallak, R. & Pereira Filho, A. J. (2011). Metodologia para análise de desempenho de simulações de  
973 sistemas convectivos na região metropolitana de São Paulo com o modelo ARPS: sensibilidade a

974 variações com os esquemas de advecção e assimilação de dados. *Revista Brasileira de*  
975 *Meteorologia*, 26, 591-608. doi:10.1590/S0102-77862011000400009

976 Hollinger, D. Y., & Richardson, A. D. (2005). Uncertainty in eddy covariance measurements and its  
977 application to physiological models. *Tree Physiology*, 25(7), 873–885.  
978 doi:10.1093/treephys/25.7.873

979 Jaafar, H., Mourad, R., & Schull, M. (2022). A global 30-m ET model (HSEB) using harmonized  
980 Landsat and Sentinel-2, MODIS and VIIRS: Comparison to ECOSTRESS ET and LST. *Remote*  
981 *Sensing of Environment*, 274, 112995. doi:10.1016/j.rse.2022.112995

982 Jia, L., Su, Z., van den Hurk, B., Menenti, M., Moene, A., De Bruin, H. A. ., ... Cuesta, A. (2003).  
983 Estimation of sensible heat flux using the Surface Energy Balance System (SEBS) and ATSR  
984 measurements. *Physics and Chemistry of the Earth, Parts A/B/C*, 28(1-3), 75–88.  
985 doi:10.1016/s1474-7065(03)00009-3

986 Kayser, R. H., Ruhoff, A., Laipelt, L., de Mello Kich, E., Roberti, D. R., de Arruda Souza, V., ... &  
987 Neale, C. M. U. (2022). Assessing geeSEBAL automated calibration and meteorological reanalysis  
988 uncertainties to estimate evapotranspiration in subtropical humid climates. *Agricultural and Forest*  
989 *Meteorology*, 314, 108775. doi:10.1016/j.agrformet.2021.108775

990 Koch, R., Almeida-Cortez, J. S., & Kleinschmit, B. (2017). Revealing areas of high nature  
991 conservation importance in a seasonally dry tropical forest in Brazil: Combination of modelled plant  
992 diversity hot spots and threat patterns. *Journal for Nature Conservation*, 35, 24–39.  
993 doi:10.1016/j.jnc.2016.11.004

994 Kustas, W., Choudhury, B. Moran, M., Reginato, R., Jackson, R., Gay, L., & Weaver, H. (1989a).  
995 Determination of sensible heat flux over sparse canopy using thermal infrared data. *Agricultural and*  
996 *Forest Meteorology*, 44(3-4), 197–216. doi:10.1016/0168-1923(89)90017-8



- 997 Kustas, W. P., Choudhury, B. J., Kunkel, K. E., & Gay, L. W. (1989b). Estimate of the aerodynamic  
998 roughness parameters over an incomplete canopy cover of cotton. *Agricultural and Forest*  
999 *Meteorology*, 46(1-2), 91-105. doi:10.1016/0168-1923(89)90114-7
- 1000 Laipelt, L., Ruhoff, A. L., Fleischmann, A. S., Kayser, R. H. B., Kich, E. de M., da Rocha, H. R., &  
1001 Neale, C. M. U. (2020). Assessment of an Automated Calibration of the SEBAL Algorithm to Estimate  
1002 Dry-Season Surface-Energy Partitioning in a Forest–Savanna Transition in Brazil. *Remote Sensing*,  
1003 12(7), 1108. doi:10.3390/rs12071108
- 1004 Laipelt, L., Henrique Bloedow Kayser, R., Santos Fleischmann, A., Ruhoff, A., Bastiaanssen, W.,  
1005 Erickson, T. A., & Melton, F. (2021). Long-term monitoring of evapotranspiration using the SEBAL  
1006 algorithm and Google Earth Engine cloud computing. *ISPRS Journal of Photogrammetry and*  
1007 *Remote Sensing*, 178, 81–96. doi:10.1016/j.isprsjprs.2021.05.018
- 1008 Lhomme, J. P., Chehbouni, A., & Monteny, B. (2000). Sensible Heat Flux-Radiometric Surface  
1009 Temperature Relationship Over Sparse Vegetation: Parameterizing B-1. *Boundary-Layer*  
1010 *Meteorology*, 97(3), 431–457. doi:10.1023/a:1002786402695
- 1011 Liao, J. J., & Lewis, J. W. (2000). A note on concordance correlation coefficient. *PDA Journal of*  
1012 *Pharmaceutical Science and Technology*, 54(1), 23-26.
- 1013 Lima, A. L. A., & Rodal, M. J. N. (2010). Phenology and wood density of plants growing in the semi-  
1014 arid region of northeastern Brazil. *Journal of Arid Environments*, 74(11), 1363–1373.  
1015 doi:10.1016/j.jaridenv.2010.05.009
- 1016 Lima, A. L. A., Sá Barretto Sampaio, E. V., Castro, C. C., Rodal, M. J. N., Antonino, A. C. D., & de  
1017 Melo, A. L. (2012). Do the phenology and functional stem attributes of woody species allow for the  
1018 identification of functional groups in the semiarid region of Brazil? *Trees*, 26(5), 1605–1616.  
1019 doi:10.1007/s00468-012-0735-2
- 1020 Lima, C. E. S. de, Costa, V. S. de O., Galvíncio, J. D., Silva, R. M. da, & Santos, C. A. G. (2021).  
1021 Assessment of automated evapotranspiration estimates obtained using the GP-SEBAL algorithm for

1022 dry forest vegetation (Caatinga) and agricultural areas in the Brazilian semiarid region. *Agricultural*  
1023 *Water Management*, 250, 106863. doi:10.1016/j.agwat.2021.106863

1024 Lin, L. K. (1989). A concordance correlation coefficient to evaluate reproducibility. *Biometrics*, 45(1),  
1025 255–268. <https://doi.org/10.2307/2532051>

1026 Liu, S., Lu, L., Mao, D., & Jia, L. (2007). Evaluating parameterizations of aerodynamic resistance to  
1027 heat transfer using field measurements. *Hydrology and Earth System Sciences*, 11(2), 769–783.  
1028 doi:10.5194/hess-11-769-2007

1029 Liu, Y., Guo, W., Huang, H., Ge, J., & Qiu, B. (2021). Estimating global aerodynamic parameters in  
1030 1982–2017 using remote-sensing data and a turbulent transfer model. *Remote Sensing of*  
1031 *Environment*, 260, 112428. doi:10.1016/j.rse.2021.112428

1032 Long, D., Gao, Y., & Singh, V. P. (2010). Estimation of daily average net radiation from MODIS data  
1033 and DEM over the Baiyangdian watershed in North China for clear sky days. *Journal of Hydrology*,  
1034 388(3–4), 217–233. doi:10.1016/j.jhydrol.2010.04.042

1035 Long, D., Singh, V. P., & Li, Z.-L. (2011). How sensitive is SEBAL to changes in input variables,  
1036 domain size and satellite sensor? *Journal of Geophysical Research: Atmospheres*, 116(D21).  
1037 Portico. doi:10.1029/2011jd016542

1038 Maia, V. A., de Souza, C. R., de Aguiar-Campos, N., Fagundes, N. C. A., Santos, A. B. M., de Paula,  
1039 G. G. P., ... dos Santos, R. M. (2020). Interactions between climate and soil shape tree community  
1040 assembly and above-ground woody biomass of tropical dry forests. *Forest Ecology and*  
1041 *Management*, 474, 118348. doi:10.1016/j.foreco.2020.118348

1042 Mallick, K., Wandera, L., Bhattarai, N., Hostache, R., Kleniewska, M., & Chormanski, J. (2018). A  
1043 critical evaluation on the role of aerodynamic and canopy–surface conductance parameterization in  
1044 SEB and SVAT models for simulating evapotranspiration: A case study in the Upper Biebrza National  
1045 Park Wetland in Poland. *Water*, 10(12), 1753. doi.org/10.3390/w10121753

1046 Marques, T. V., Mendes, K., Mutti, P., Medeiros, S., Silva, L., Perez-Marin, A. M., ... Bezerra, B.  
1047 (2020). Environmental and biophysical controls of evapotranspiration from Seasonally Dry Tropical  
1048 Forests (Caatinga) in the Brazilian Semiarid. *Agricultural and Forest Meteorology*, 287, 107957.  
1049 doi:10.1016/j.agrformet.2020.107957

1050 McShane, R. R., Driscoll, K. P., & Sando, R. (2017). A review of surface energy balance models for  
1051 estimating actual evapotranspiration with remote sensing at high spatiotemporal resolution over  
1052 large extents. *Scientific Investigations Report*. doi:10.3133/sir20175087

1053 Medeiros, R., Andrade, J., Ramos, D., Moura, M., Pérez-Marin, A., dos Santos, C., ... Cunha, J.  
1054 (2022). Remote Sensing Phenology of the Brazilian Caatinga and Its Environmental Drivers. *Remote  
1055 Sensing*, 14(11), 2637. doi:10.3390/rs14112637

1056 Meier, R., Davin, E. L., Swenson, S. C., Lawrence, D. M., & Schwaab, J. (2019). Biomass heat  
1057 storage dampens diurnal temperature variations in forests. *Environmental Research Letters*, 14(8),  
1058 084026. doi:10.1088/1748-9326/ab2b4e

1059 Melo, D. C. D., Anache, J. A. A., Borges, V. P., Miralles, D. G., Martens, B., Fisher, J. B., ...  
1060 Wendland, E. (2021). Are remote sensing evapotranspiration models reliable across South American  
1061 ecoregions? *Water Resources Research*, 57(11). doi:10.1029/2020wr028752

1062 Mhaweji, M., Caiserman, A., Nasrallah, A., Dawi, A., Bachour, R., & Faour, G. (2020). Automated  
1063 evapotranspiration retrieval model with missing soil-related datasets: The proposal of SEBALL.  
1064 *Agricultural Water Management*, 229, 105938. doi:10.1016/j.agwat.2019.105938

1065 Miles, L., Newton, A. C., DeFries, R. S., Ravillious, C., May, I., Blyth, S., ... Gordon, J. E. (2006). A  
1066 global overview of the conservation status of tropical dry forests. *Journal of Biogeography*, 33(3),  
1067 491–505. doi:10.1111/j.1365-2699.2005.01424.x

1068 Miranda, R. Q., Nóbrega, R. L. B., Moura, M. S. B., Raghavan, S., & Galvíncio, J. D. (2020). Realistic  
1069 and simplified models of plant and leaf area indices for a seasonally dry tropical forest. *International*

1070 Journal of Applied Earth Observation and Geoinformation, 85, 101992.  
1071 doi:10.1016/j.jag.2019.101992

1072 Miranda, R. D. Q., Galvencio, J. D., Morais, Y. C. B., Moura, M. S. B. D., Jones, C. A., & Srinivasan,  
1073 R. (2018). Dry forest deforestation dynamics in Brazil's Pontal Basin. *Revista Caatinga*, 31, 385-395.  
1074 doi:10.1590/1983-21252018v31n215rc

1075 Mohan, M. M. P., Kanchirapuzha, R., & Varma, M. R. R. (2020a). Review of approaches for the  
1076 estimation of sensible heat flux in remote sensing-based evapotranspiration models. *Journal of*  
1077 *Applied Remote Sensing*, 14(04). doi:10.1117/1.jrs.14.041501

1078 Mohan, M. P.; Kanchirapuzha, R., & Varma, M. R. R. (2020b). Integration of soil moisture as an  
1079 auxiliary parameter for the anchor pixel selection process in SEBAL using Landsat 8 and Sentinel-  
1080 1A images. *International Journal of Remote Sensing*, 41(3), 1214-1231.

1081 Moro, M. F., Silva, I. A., Araújo, F. S. de, Nic Lughadha, E., Meagher, T. R., & Martins, F. R. (2015).  
1082 The role of edaphic environment and climate in structuring phylogenetic pattern in Seasonally Dry  
1083 Tropical Plant Communities. *PLOS ONE*, 10(3), e0119166. doi:10.1371/journal.pone.0119166

1084 Moro, M. F., Nic Lughadha, E., de Araújo, F. S., & Martins, F. R. (2016). A Phytogeographical  
1085 Metaanalysis of the Semiarid Caatinga domain in Brazil. *The Botanical Review*, 82(2), 91–148.  
1086 doi:10.1007/s12229-016-9164-z

1087 Mu, Q., Zhao, M., & Running, S. W. (2011). Improvements to a MODIS global terrestrial  
1088 evapotranspiration algorithm. *Remote Sensing of Environment*, 115(8), 1781–1800.  
1089 doi:10.1016/j.rse.2011.02.019

1090 Muñoz Sabater, J., (2019): ERA5-Land hourly data from 1981 to present. Copernicus Climate  
1091 Change Service (C3S) Climate Data Store (CDS). (Accessed on 23-Feb-2022),  
1092 doi:10.24381/cds.e2161bac

1093 Mutti, P. R., da Silva, L. L., Medeiros, S. de S., Dubreuil, V., Mendes, K. R., Marques, T. V., ...  
1094 Bezerra, B. G. (2019). Basin scale rainfall-evapotranspiration dynamics in a tropical semiarid

1095 environment during dry and wet years. *International Journal of Applied Earth Observation and*  
1096 *Geoinformation*, 75, 29–43. doi:10.1016/j.jag.2018.10.007

1097 Murray, T., and Verhoef, A. (2007) Moving towards a more mechanistic approach in the  
1098 determination of soil heat flux from remote measurements. II. Diurnal shape of soil heat flux.  
1099 *Agricultural and Forest Meteorology*, 147: 88-97.

1100 Nash, J. E., & Sutcliffe, J. V. (1970). River flow forecasting through conceptual models part I - A  
1101 discussion of principles. *Journal of Hydrology*, 10(3), 282–290. doi:10.1016/0022-1694(70)90255-6

1102 Oliveira, M. L., Santos, C. A. C., Oliveira, G., Perez-Marin, A. M., & Santos, C. A. G. (2021). Effects  
1103 of human-induced land degradation on water and carbon fluxes in two different Brazilian dryland soil  
1104 covers. *Science of the Total Environment*, 792, 148458. doi:10.1016/j.scitotenv.2021.148458

1105 Owen, P. R., & Thomson, W. R. (1963). Heat transfer across rough surfaces. *Journal of Fluid*  
1106 *Mechanics*, 15(3), 321–334. doi:10.1017/s0022112063000288

1107 Paloschi, R. A., Ramos, D. M., Ventura, D. J., Souza, R., Souza, E., Morellato, L. P. C., ... Borma,  
1108 L. D. S. (2020). Environmental drivers of water use for Caatinga woody plant species: Combining  
1109 remote sensing phenology and sap flow measurements. *Remote Sensing*, 13(1), 75.  
1110 doi:10.3390/rs13010075

1111 Paul, G., Gowda, P. H., Vara Prasad, P. V., Howell, T. A., Staggenborg, S. A., & Neale, C. M. U.  
1112 (2013). Lysimetric evaluation of SEBAL using high resolution airborne imagery from BEAREX08.  
1113 *Advances in Water Resources*, 59, 157–168. doi:10.1016/j.advwatres.2013.06.003

1114 Paul, G., Gowda, P. H., Vara Prasad, P. V., Howell, T. A., Aiken, R. M., & Neale, C. M. U. (2014).  
1115 Investigating the influence of roughness length for heat transport (zoh) on the performance of SEBAL  
1116 in semi-arid irrigated and dryland agricultural systems. *Journal of Hydrology*, 509, 231–244.  
1117 doi:10.1016/j.jhydrol.2013.11.040

1118 Paulson, C. A. (1970). The mathematical representation of wind speed and temperature profiles in  
1119 the unstable atmospheric surface layer. *Journal of Applied Meteorology and Climatology*, 9(6), 857-  
1120 861. doi:10.1175/1520-0450(1970)009%3C0857:tmrows%3E2.0.co;2

1121 Pennington, R. T., Lewis, G. P., & Ratter, J. A. (Eds.). (2006). An overview of the plant diversity,  
1122 biogeography and conservation of Neotropical Savannas and Seasonally Dry Forests. *Neotropical*  
1123 *Savannas and Seasonally Dry Forests*, 1–29. doi:10.1201/9781420004496-1

1124 Pennington, R. T., Lavin, M., & Oliveira-Filho, A. (2009). Woody plant diversity, evolution, and  
1125 ecology in the Tropics: Perspectives from Seasonally Dry Tropical Forests. *Annual Review of*  
1126 *Ecology, Evolution, and Systematics*, 40(1), 437–457. doi:10.1146/annurev.ecolsys.110308.120327

1127 Pennington, R. T., Lehmann, C. E. R., & Rowland, L. M. (2018). Tropical savannas and dry forests.  
1128 *Current Biology*, 28(9), R541–R545. doi:10.1016/j.cub.2018.03.014

1129 Potapov, P., Li, X., Hernandez-Serna, A., Tyukavina, A., Hansen, M. C., Kommareddy, A., ... Hofton,  
1130 M. (2021). Mapping global forest canopy height through integration of GEDI and Landsat data.  
1131 *Remote Sensing of Environment*, 253, 112165. doi:10.1016/j.rse.2020.112165

1132 Priestley, C. H. B., & Taylor, R. J. (1972). On the assessment of surface heat flux and evaporation  
1133 using large-scale parameters. *Monthly Weather Review*, 100(2), 81–92. doi:10.1175/1520-  
1134 0493(1972)100<0081:otaosh>2.3.co;2

1135 Queiroz, L. P., Cardoso, D., Fernandes, M. F., & Moro, M. F. (2017). Diversity and evolution of  
1136 flowering plants of the Caatinga domain. *Caatinga*, 23–63. doi:10.1007/978-3-319-68339-3\_2

1137 Queiroz, M. G. D., Silva, T. G. F. D., Souza, C. A. A. D., Jardim, A. M. D. R. F., Araújo Júnior, G. D.  
1138 N., Souza, L. S. B. D., & Moura, M. S. B. D. (2020). Composition of Caatinga species under anthropic  
1139 disturbance and its correlation with rainfall partitioning. *Floresta e Ambiente*, 28. doi:10.1590/2179-  
1140 8087-FLORAM-2019-0044

1141 Ramoelo, A., Majozi, N., Mathieu, R., Jovanovic, N., Nickless, A., & Dziki, S. (2014). Validation of  
1142 global evapotranspiration product (MOD16) using flux tower data in the African Savanna, South  
1143 Africa. *Remote Sensing*, 6(8), 7406–7423. doi:10.3390/rs6087406

1144 Rasp, S., Pritchard, M. S., & Gentile, P. (2018). Deep learning to represent subgrid processes in  
1145 climate models. *Proceedings of the National Academy of Sciences*, 115(39), 9684–9689.  
1146 doi:10.1073/pnas.1810286115

1147 Raupach, M. R. (1992). Drag and drag partition on rough surfaces. *Boundary-Layer Meteorology*,  
1148 60(4), 375–395. doi.org/10.1007/bf00155203

1149 Raupach, M. R. (1994). Simplified expressions for vegetation roughness length and zero-plane  
1150 displacement as functions of canopy height and area index. *Boundary-Layer Meteorology*, 71(1–2),  
1151 211–216. doi:10.1007/bf00709229

1152 Roberts, W., Williams, G. P., Jackson, E., Nelson, E. J., & Ames, D. P. (2018). Hydrostats: A Python  
1153 package for characterizing errors between observed and predicted time series. *Hydrology*, 5(4), 66.  
1154 doi:10.3390/hydrology5040066

1155 Rodell, M., Houser, P. R., Jambor, U., Gottschalck, J., Mitchell, K., Meng, C.-J., ... Toll, D. (2004).  
1156 The Global Land Data Assimilation System. *Bulletin of the American Meteorological Society*, 85(3),  
1157 381–394. doi:10.1175/bams-85-3-381

1158 Running, S., Mu, Q., Zhao, M. (2017). MOD16A2 MODIS/Terra Net Evapotranspiration 8-Day L4  
1159 Global 500m SIN Grid V006 [Data set]. NASA EOSDIS Land Processes DAAC. Accessed 23-Feb-  
1160 2022 from doi:10.5067/MODIS/MOD16A2.006

1161 Sahnoun, F., Abderrahmane, H., Kaddour, M., Abdelkader, K., Mohamed, B., & Castro, T. A. H. D.  
1162 (2021). Application of SEBAL and T s/VI trapezoid models for estimating actual evapotranspiration  
1163 in the Algerian Semi-Arid Environment to improve agricultural water management. *Revista Brasileira  
1164 de Meteorologia*, 36, 219-236. doi:10.1590/0102-77863610020

1165 Salazar-Martínez, D., Holwerda, F., Holmes, T. R. H., Yépez, E. A., Hain, C. R., Alvarado-Barrientos,  
1166 S., ... Vivoni, E. R. (2022). Evaluation of remote sensing-based evapotranspiration products at low-  
1167 latitude eddy covariance sites. *Journal of Hydrology*, 610, 127786.  
1168 doi:10.1016/j.jhydrol.2022.127786

1169 Santos, R. M., Oliveira-Filho, A. T., Eisenlohr, P. V., Queiroz, L. P., Cardoso, D. B. O. S., & Rodal,  
1170 M. J. N. (2012). Identity and relationships of the Arboreal Caatinga among other floristic units of  
1171 seasonally dry tropical forests (SDTFs) of north-eastern and Central Brazil. *Ecology and Evolution*,  
1172 2(2), 409–428. doi:10.1002/ece3.91

1173 Santos, M. G., Oliveira, M. T., Figueiredo, K. V., Falcão, H. M., Arruda, E. C. P., Almeida-Cortez, J.,  
1174 ... Antonino, A. C. D. (2014). Caatinga, the Brazilian dry tropical forest: can it tolerate climate  
1175 changes? *Theoretical and Experimental Plant Physiology*, 26(1), 83–99. doi:10.1007/s40626-014-  
1176 0008-0

1177 Santos, C. A. C., Mariano, D. A., das Chagas A. do Nascimento, F., da C. Dantas, F. R., de Oliveira,  
1178 G., Silva, M. T., ... Neale, C. M. U. (2020). Spatio-temporal patterns of energy exchange and  
1179 evapotranspiration during an intense drought for drylands in Brazil. *International Journal of Applied*  
1180 *Earth Observation and Geoinformation*, 85, 101982. doi:10.1016/j.jag.2019.101982

1181 Schaaf, C., & Wang, Z. (2015). MCD43A4 MODIS/Terra+Aqua BRDF/Albedo Nadir BRDF Adjusted  
1182 Ref Daily L3 Global - 500m V006 [Data set]. NASA EOSDIS Land Processes DAAC. Accessed 23-  
1183 Feb-2022. doi:10.5067/MODIS/MCD43A4.006

1184 Senay, G. B., Bohms, S., Singh, R. K., Gowda, P. H., Velpuri, N. M., Alemu, H., & Verdin, J. P.  
1185 (2013). Operational evapotranspiration mapping using remote sensing and weather datasets: A new  
1186 parameterization for the SSEB approach. *JAWRA Journal of the American Water Resources*  
1187 *Association*, 49(3), 577–591. Portico. <https://doi.org/10.1111/jawr.12057>

1188 Senay, G. B., Friedrichs, M., Morton, C., Parrish, G. E., Schauer, M., Khand, K., ... & Huntington, J.  
1189 (2022). Mapping actual evapotranspiration using Landsat for the conterminous United States:



1190 Google Earth Engine implementation and assessment of the SSEBop model. *Remote Sensing of*  
1191 *Environment*, 275, 113011. doi:10.1016/j.rse.2022.113011

1192 Senkondo, W., Munishi, S. E., Tumbo, M., Nobert, J., & Lyon, S. W. (2019). Comparing remotely-  
1193 sensed surface energy balance evapotranspiration estimates in heterogeneous and data-limited  
1194 regions: a case study of Tanzania's Kilombero Valley. *Remote Sensing*, 11(11), 1289.  
1195 doi:10.3390/rs11111289

1196 Shuttleworth, W. J. (2012). *Terrestrial hydrometeorology*. John Wiley & Sons.

1197 Silva, A. M., da Silva, R. M., & Santos, C. A. G. (2019). Automated surface energy balance algorithm  
1198 for land (ASEBAL) based on automating endmember pixel selection for evapotranspiration  
1199 calculation in MODIS orbital images. *International Journal of Applied Earth Observation and*  
1200 *Geoinformation*, 79, 1–11. doi:10.1016/j.jag.2019.02.012

1201 Silva, J. M. C.; LEAL, I.R.; Tabarelli, M. (Ed.). (2017a). *Caatinga: the largest tropical dry forest region*  
1202 *in South America*. Springer.

1203 Silva, P. F. da, Lima, J. R. de S., Antonino, A. C. D., Souza, R., Souza, E. S. de, Silva, J. R. I., &  
1204 Alves, E. M. (2017b). Seasonal patterns of carbon dioxide, water and energy fluxes over the  
1205 Caatinga and grassland in the semi-arid region of Brazil. *Journal of Arid Environments*, 147, 71–82.  
1206 doi:10.1016/j.jaridenv.2017.09.003

1207 Singh, R. K., & Irmak, A. (2011). Treatment of anchor pixels in the METRIC model for improved  
1208 estimation of sensible and latent heat fluxes. *Hydrological Sciences Journal*, 56(5), 895–906.  
1209 doi:10.1080/02626667.2011.587424

1210 Singh, R. K., Liu, S., Tieszen, L. L., Suyker, A. E., & Verma, S. B. (2012). Estimating seasonal  
1211 evapotranspiration from temporal satellite images. *Irrigation Science*, 30(4), 303-313.  
1212 doi:10.1007/s00271-011-0287-z

- 1213 Souza, L. S. B. de, Moura, M. S. B. de, Sedyama, G. C., & Silva, T. G. F. da. (2015). Balanço de  
1214 energia e controle biofísico da evapotranspiração na Caatinga em condições de seca intensa.  
1215 Pesquisa Agropecuária Brasileira, 50(8), 627–636. doi:10.1590/s0100-204x2015000800001
- 1216 Stewart, J. B., Kustas, W. P., Humes, K. S., Nichols, W. D., Moran, M. S., & de Bruin, H. A. (1994).  
1217 Sensible heat flux-radiometric surface temperature relationship for eight semiarid areas. Journal of  
1218 Applied Meteorology and Climatology, 33(9), 1110-1117. doi:10.1175/1520-  
1219 0450(1994)033%3C1110:shfrst%3E2.0.co;2
- 1220 Su, Z., Schmugge, T., Kustas, W. P., & Massman, W. J. (2001). An evaluation of two models for  
1221 estimation of the roughness height for heat transfer between the land surface and the atmosphere.  
1222 Journal of Applied Meteorology, 40(11), 1933-1951. doi:10.1175/1520-  
1223 0450(2001)040%3C1933:aeotmf%3E2.0.co;2
- 1224 Su, Z. (2002). The Surface Energy Balance System (SEBS) for estimation of turbulent heat fluxes.  
1225 Hydrology and Earth System Sciences, 6(1), 85–100. doi:10.5194/hess-6-85-2002
- 1226 Swenson, S. C., Burns, S. P., & Lawrence, D. M. (2019). The Impact of Biomass Heat Storage on  
1227 the Canopy Energy Balance and Atmospheric Stability in the Community Land Model. Journal of  
1228 Advances in Modeling Earth Systems, 11(1), 83–98. Portico. doi:10.1029/2018ms001476
- 1229 Teixeira, A. D. C., Bastiaanssen, W. G., Ahmad, M., & Bos, M. G. (2009). Reviewing SEBAL input  
1230 parameters for assessing evapotranspiration and water productivity for the Low-Middle Sao  
1231 Francisco River basin, Brazil: Part A: Calibration and validation. Agricultural and Forest Meteorology,  
1232 149(3-4), 462-476. doi:10.1016/j.agrformet.2008.09.016
- 1233 Thom, A. S. (1972). Momentum, mass and heat exchange of vegetation. Quarterly Journal of the  
1234 Royal Meteorological Society, 98(415), 124–134. doi:10.1002/qj.49709841510
- 1235 Tomasella, J., Silva Pinto Vieira, R. M., Barbosa, A. A., Rodriguez, D. A., Oliveira Santana, M. de, &  
1236 Sestini, M. F. (2018). Desertification trends in the Northeast of Brazil over the period 2000–2016.

1237 International Journal of Applied Earth Observation and Geoinformation, 73, 197–206.  
1238 doi:10.1016/j.jag.2018.06.012

1239 Trebs, I., Mallick, K., Bhattarai, N., Sulis, M., Cleverly, J., Woodgate, W., Silberstein, R., Hinko-  
1240 Najera, N., Beringer, J., Meyer, W. S., Su, Z., & Boulet, G. (2021). The role of aerodynamic  
1241 resistance in thermal remote sensing-based evapotranspiration models. EGU General Assembly.  
1242 doi.org/10.5194/egusphere-egu21-2186Remote Sensing of Environment, 264, 112602.  
1243 doi:10.1016/j.rse.2021.112602

1244 Trezza, R. (2006). Evapotranspiration from a remote sensing model for water management in an  
1245 irrigation system in Venezuela. *Interciencia*, 31(6), 417-423

1246 Trezza, R., Allen, R., & Tasumi, M. (2013). Estimation of Actual Evapotranspiration along the Middle  
1247 Rio Grande of New Mexico Using MODIS and Landsat Imagery with the METRIC Model. *Remote*  
1248 *Sensing*, 5(10), 5397–5423. doi:10.3390/rs5105397

1249 Troufleau, D., Lhomme, J. P., Monteny, B., & Vidal, A. (1997). Sensible heat flux and radiometric  
1250 surface temperature over sparse Sahelian vegetation. I. An experimental analysis of the kB–1  
1251 parameter. *Journal of Hydrology*, 188, 815-838. doi:10.1016/s0022-1694(96)03172-1

1252 Verhoef, A., De Bruin, H. A. R., & Van Den Hurk, B. J. J. M. (1997a). Some practical notes on the  
1253 parameter kB–1 for sparse vegetation. *Journal of Applied Meteorology*, 36(5), 560-572.  
1254 doi:10.1175/1520-0450(1997)036%3C0560:spnotp%3E2.0.co;2

1255 Verhoef, A., McNaughton, K. G., & Jacobs, A. F. G. (1997b). A parameterization of momentum  
1256 roughness length and displacement height for a wide range of canopy densities. *Hydrology and Earth*  
1257 *System Sciences*, 1(1), 81–91. doi:10.5194/hess-1-81-1997

1258 Wang, C., Yang, J., Myint, S. W., Wang, Z.-H., & Tong, B. (2016). Empirical modeling and spatio-  
1259 temporal patterns of urban evapotranspiration for the Phoenix metropolitan area, Arizona. *GIScience*  
1260 *& Remote Sensing*, 53(6), 778–792. doi:10.1080/15481603.2016.1243399

- 1261 Wilson, K., Goldstein, A., Falge, E., Aubinet, M., Baldocchi, D., Berbigier, P., ... Verma, S. (2002).  
1262 Energy balance closure at FLUXNET sites. *Agricultural and Forest Meteorology*, 113(1-4), 223–243.  
1263 doi:10.1016/s0168-1923(02)00109-0
- 1264 WRB, I.W.G., 2006. World reference base for soil resources 2006, 2nd ed. In: FAO (ed.), *World Soil*  
1265 *Resources Reports No. 103*, Rome. ISBN 92-5-105511-4.
- 1266 Wu, Q. (2020). geemap: A Python package for interactive mapping with Google Earth Engine.  
1267 *Journal of Open Source Software*, 5(51), 2305. doi:10.21105/joss.02305
- 1268 Yin, L., Wang, X., Feng, X., Fu, B., & Chen, Y. (2020). A comparison of SSEBop-Model-Based  
1269 evapotranspiration with eight evapotranspiration products in the Yellow River Basin, China. *Remote*  
1270 *Sensing*, 12(16), 2528. doi:10.3390/rs12162528
- 1271 Zhang, Y., Kong, D., Gan, R., Chiew, F. H. S., McVicar, T. R., Zhang, Q., & Yang, Y. (2019). Coupled  
1272 estimation of 500 m and 8-day resolution global evapotranspiration and gross primary production in  
1273 2002–2017. *Remote Sensing of Environment*, 222, 165–182. doi:10.1016/j.rse.2018.12.031
- 1274 Zhao, M., Heinsch, F. A., Nemani, R. R., & Running, S. W. (2005). Improvements of the MODIS  
1275 terrestrial gross and net primary production global data set. *Remote sensing of Environment*, 95(2),  
1276 164-176. doi:10.1016/j.rse.2004.12.011